Supplementary materials: Tracking of atomic planes in Atom Probe Tomography

Sebastian Koelling,[1*] Simone Assali,[1] Guillaume Nadal,[1]
Dieter Isheim,[2] David N. Seidman,[2] Oussama Moutanabbir[1]

[1]Department of Engineering Physics, École Polytechnique de Montréal,
C. P. 6079, Succ. Centre-Ville, Montréal, QC H3C 3A7, Canada
[2]Department of Materials Science & Engineering, Northwestern University,
Evanston, IL 60208, USA

*To whom correspondence should be addressed; E-mail: sebastian.koelling@polymtl.ca.

1 The plane finding algorithm

1.1 Setting the Parameters

As discussed in the main text a number of parameters can be chosen when the plane finding algorithm is applied to an APT data set.

The first two parameters are related to the detector space reconstruction (DSR) and are the size of the window used for the reconstruction and the step the window is moved after each reconstruction. Note, that for now we limited ourselves to a square window that is put on a grid generated using the full Cartesian product created from the two sets of points on the x- and y-axis respectively in the following way: move with positive step-size along the axis from the minimum coordinate to as close as possible to maximum coordinate and then back from the maximum coordinate to as close as possible to minimum using negative step-size. For all data sets shown here, we have used a 10x10 mm wide square window for the reconstruction and a

3 mm step-size.

The next two parameters are related to the FFT and are the grid dimensions for the FFT and the bins per unit of length for the FFT, effectively the maximum resolution in Fourier space. Again, we limit ourselves to grids with an equal number of bins in x and y. For the data shown here we used 50x50 grids, 60x60 or 70x70 grids. For the analysis of the aluminum data a 70x70 grid is used to reveal the high index poles that are comparatively small in spatial extend. The reconstruction parameters for the semiconductor hetero-structure are found using two different analyses, the one with the larger steps of 5e6 ions along the depth axis is done with a 60x60 grid and the one with the smaller steps of 3e6 ions is done with a 50x50 grid. We find that the differences are marginal. For the FFT bins per unit length we use 1000/unit length a number that is only meaningful in association with the length of the DSR.

The length of the DSR is always set to 10 units here. This is essentially a dummy parameter that is just helpful to keep around. First, it is helpful to have all DSR have the same size so the positions of FFT signals can be readily compared throughout the whole data set. Second, in association with the FFT bins per unit length this sets the resolution in Fourier space. For these reason it is useful to put this length to the approximate size of a single depths bin in nm as then 1/(FFT position) in nm is approximately the spacing of the planes and hence the resolution in real space is approximately 1/1000 nm or 0.1 pm. In practical terms this means we can choose depth bins of up to 1000 nm in length before the resolution in Fourier space is less than 0.1 nm; giving us a large margin of error.

The final parameter used in the work shown here is the step-size along the depth- or time axis given in number of ions. We used steps of 2×10^6 ions for the reconstruction of the aluminum data set in Fig. 1 and section S2, 3×10^6 ions and 5×10^6 ions for the extraction of the reconstruction parameters of the semiconductor hetero-structure in Fig. 3 and 5×10^6 ions for the analyses of both the Ge and SiGeSn volumes in Fig. 2 and section S3. Note, that the

algorithm can just be started with a pair of lists giving the start and the end of each depth bin and is hence fully flexible with respect to the depth bins.

A final option that has not been made use of in this manuscript is to only do the FFT for a limited number of elements or a single element rather than all elements in the volume.

1.2 Additional output

In the main text we exclusively focus on the signal strength of the FFT for data analysis where signal strength is defined as the number of standard deviations the highest peak is above the mean signal (see Fig. 1c). However, as already mentioned we typically do several 10 FFTs per grid point during the analysis *for each* depth bin. This is shown for the aluminum data set in Fig. S1, 'fftcounts' shows how many FFTs were carried out in each square of the Fourier grid.

Given the multitude of FFTs we can now plot averages and variances of relevant variables as shown in Fig. S1. All maps behave like we expect. When planes are present, the average and maximum signal is high, the average of the absolute value of the FFT is high, the variance in the position of the main FFT peak is low and the average position in Fourier space is relatively small as due to the choice of parameters discussed above, real plane signals are likely to end up between bin 10 and 1000 in the 10000 bin wide Fourier space.

1.3 Post-processing of the signal map: The highest peaks

For the further automated processing of the data it is helpful to employ a peak search on the signal map. For all the analyses done here we employed a topological peak-search based on persistent homology (*1*). So the highest peaks in the maps are the highest peaks with respect to this kind of search.

The idea of this approach can be visualized by imagining that the map is fully covered in water and the water is slowly removed. The n^{th} highest peaks are the first n pieces of land to

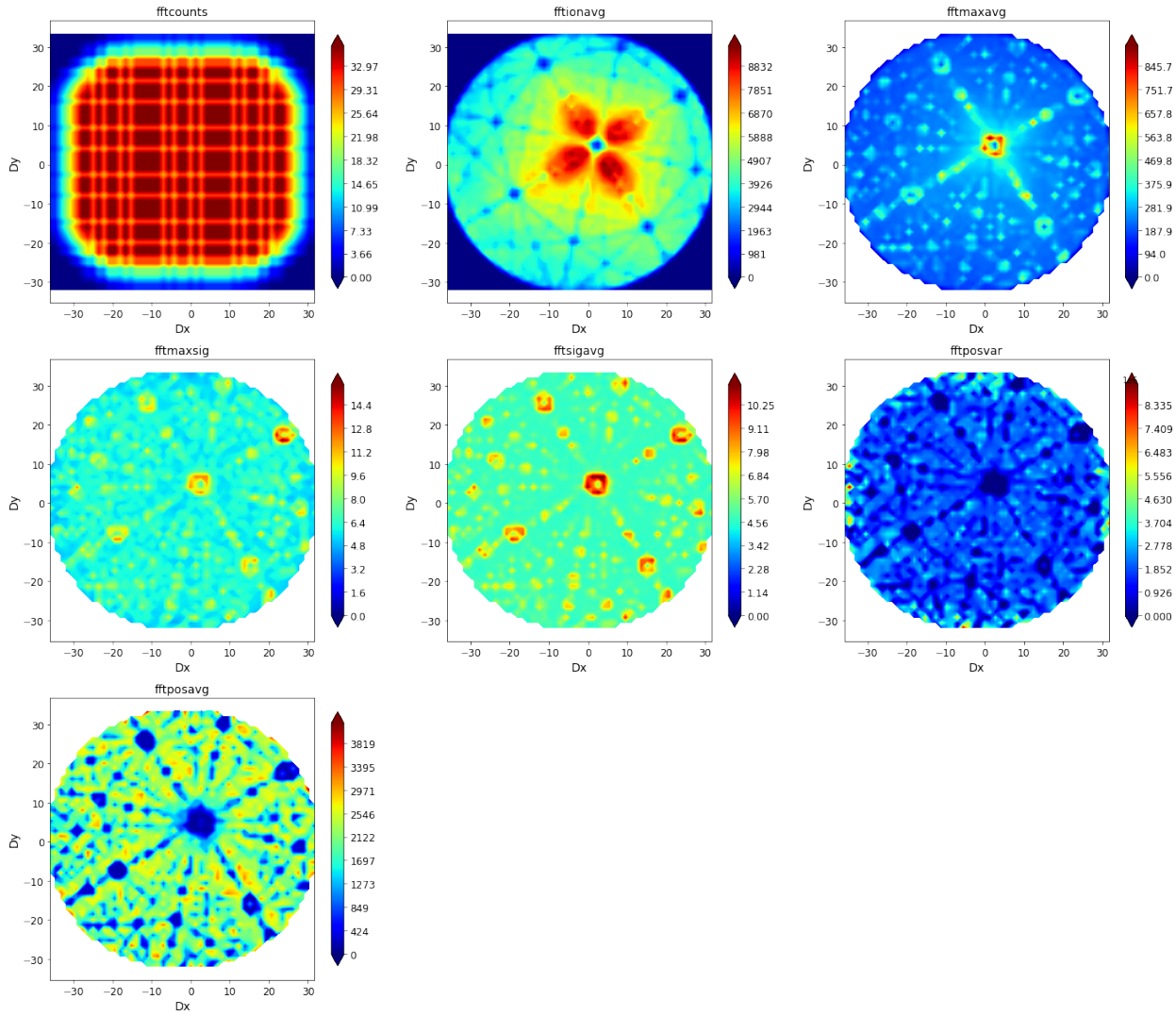

Figure S1: **Additional data maps:** The FFT analysis allows to generate a variety of maps, like the number of FFTs calculated on each square of the fft grid (fftcounts), the number of ions in each square (fftionavg), the average absolute value of the FFT signal (fftmaxavg), the absolute maximum signal of the highest FFT peak (fftmaxsig), the average signal of the highest FFT peak (fftsigavg) which is used for all analyses in the main manuscript, the average position of the highest fft peak (fftposavg) and the variance on the position in the highest fft peak (fftposvar).

be revealed from the water that are in isolation upon reveal, i.e. are not connected to portions of land already uncovered beforehand. Points with high signal strength that are neighboring on points with even higher signal strength are not considered separate peaks but are considered to

be part of the same peak as the neighbor.

2 Atomic planes imaged in voltage pulsed aluminum

The aluminum sample as measured on a LEAP 5000 XS in voltage pulse mode with a pulse fraction of 20 % and a base temperature of 50 K for approximately 10e6 ions at a voltage between 5.5 and 6 kV. We use the procedure described in the main manuscript to reconstruct the data set. This shows that the tip has starting radius of approximately 80 nm and a cone angle of approximately 24°. The 10e6 ions result in the removal of about 25 nm of material.

The map shown in Fig. S2 shows the position and identification of 130 plane sets found in this data set. The position of each plane set is marked with a 'x' at the position where the algorithm found it. The theoretical position of each plane set based on the hemispherical assumptions used in the current standard reconstruction algorithm (*2, 3*) is marked with an 'o' in the same color. For each of the 130 plane sets the spatial distribution map (SDMs) (*4*) is shown in supplementary fig. S3 proving that the plane set is indeed imaged in the region predicted by the algorithm. For each plane set the expected and measured plane spacing and angle with respect to the $(0\ 0\ 4)$-pole are shown.

Plane sets are filtered from the reconstructed volume by looking for the highest signal in a three-dimensional Fourier space created by a discrete Fourier transform as described in (*5*). The length of the vector in the 3D Fourier space is used to calculate the lattice spacing. The angles between the respective vectors in Fourier space are used to calculate the angles between the plane sets. Finally, the vector is used to rotate the plane set isogonally into the xz-plane and create the SDMs shown in supplementary fig. S3.

Interestingly, in some regions overlapping plane sets can be found as can be seen in the SDMs of the $(0\ \overline{6}\ 8)$ and $(\overline{3}\ 3\ 7)$ in supplementary fig. S3. When filtering these planes, the Fourier space mapped (*5*) is manually restricted to higher frequencies (shorter distances) to avoid finding the lower index pole planes with a larger plane distance instead of the higher

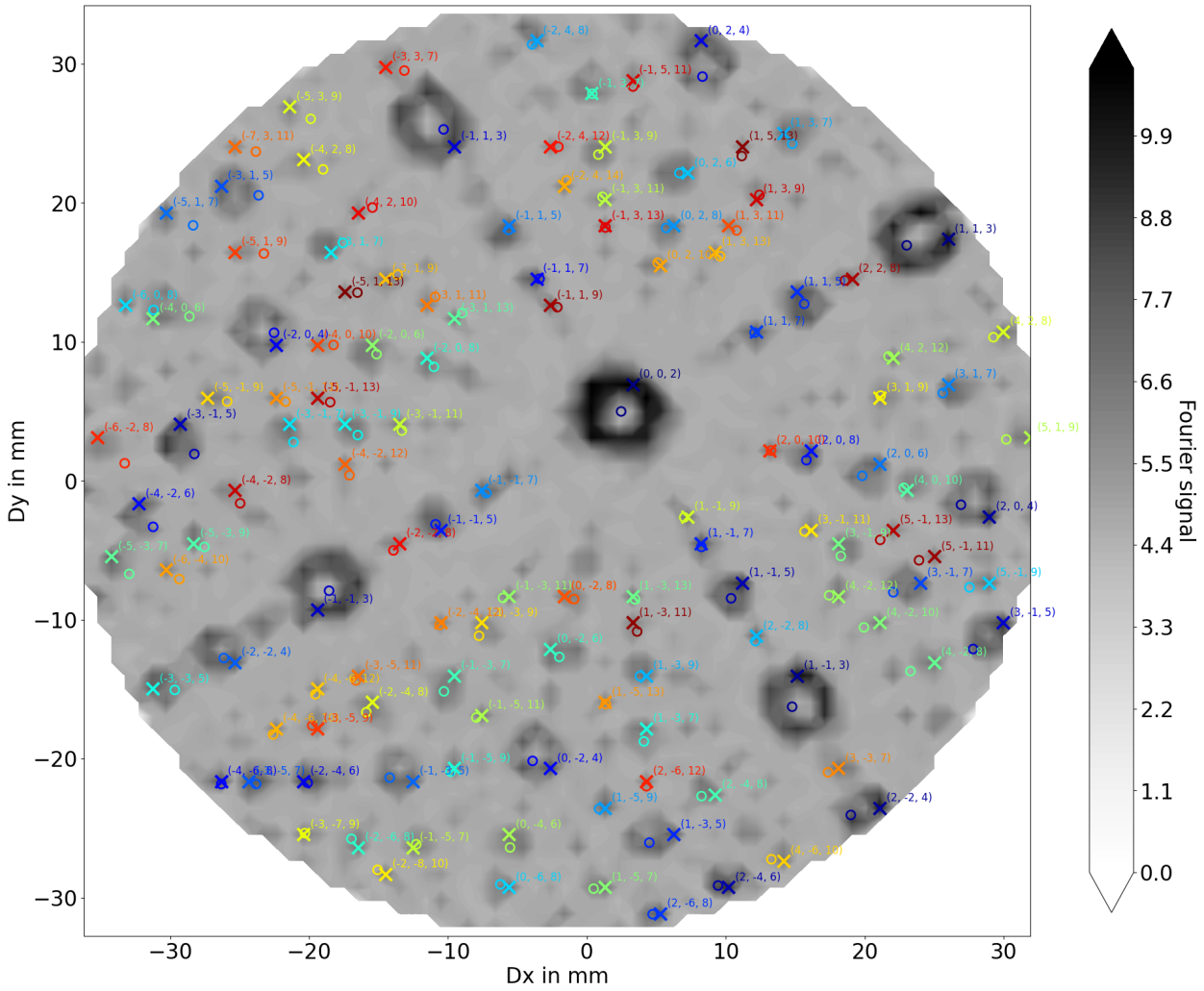

Figure S2: **Pole map of aluminum:** The position of 130 plane sets detected by the algorithm marked with an 'x' and identified by their respective Miller indices. The theoretical position of the respective poles on a hemisphere are marked with an 'o'. Spatial distribution maps for all 130 plane sets are shown in supplementary fig. S3.

index pole with a smaller inter-plane distance. Mapping out these overlaps in detail will be interesting as comparing the fidelity of different plane sets in the same region allows to directly measure the lateral resolution achieved in the measurement (*5*).

{002}

$d = 0.198\ nm$
$\theta_{004} = 0°$

$d = 0.196\ nm$ $\theta_{004} = 0°$

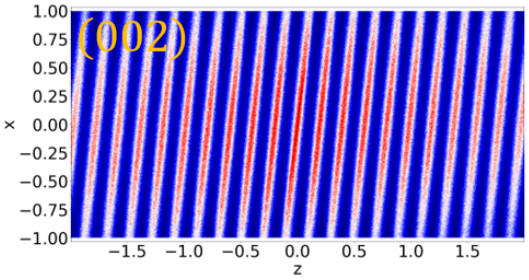

{113}

$d = 0.122\ nm$
$\theta_{004} = 25.24°$

$d = 0.114\ nm$ $\theta_{004} = 24.26°$

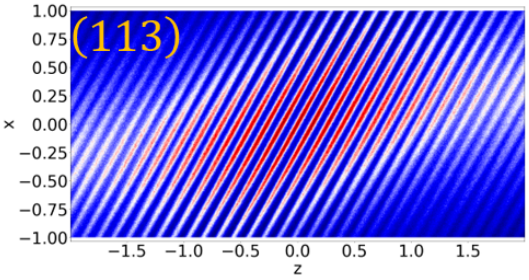

$d = 0.116\ nm$ $\theta_{004} = 25.38°$

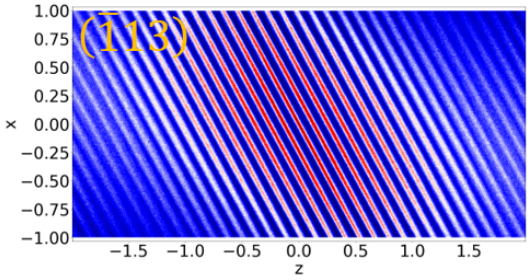

$d = 0.125\ nm$ $\theta_{004} = 25.45°$

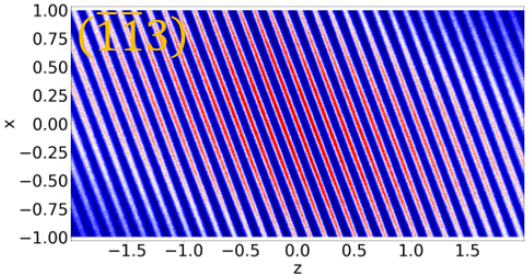

$d = 0.123\ nm$ $\theta_{004} = 24.99°$

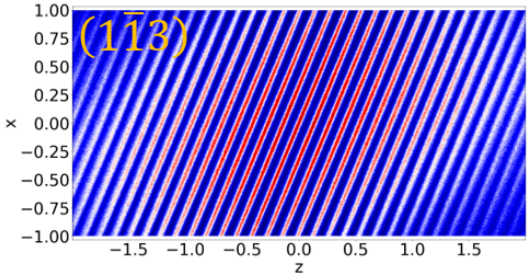

{115}

$d = 0.078\ nm$
$\theta_{004} = 15.79°$

$d = 0.074\ nm$ $\theta_{004} = 15.85°$

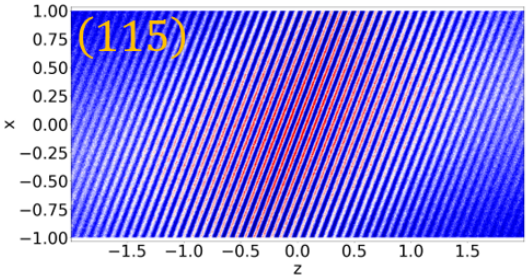

$d = 0.072\ nm$ $\theta_{004} = 16.31°$

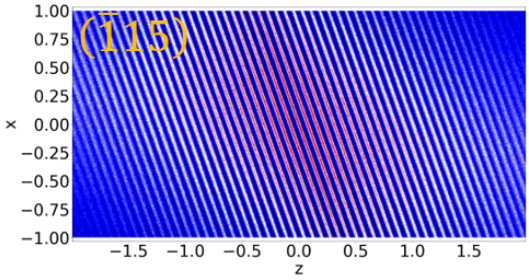

$d = 0.077\ nm$ $\theta_{004} = 16.40°$

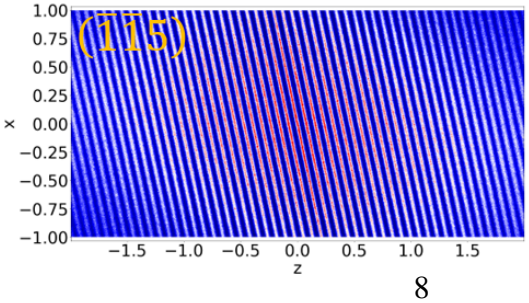

$d = 0.077\ nm$ $\theta_{004} = 16.02°$

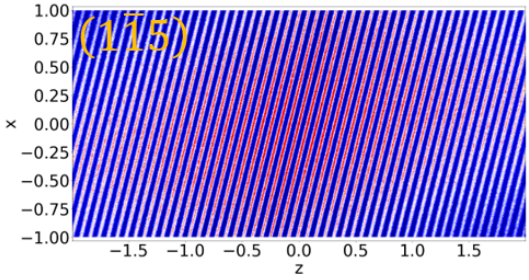

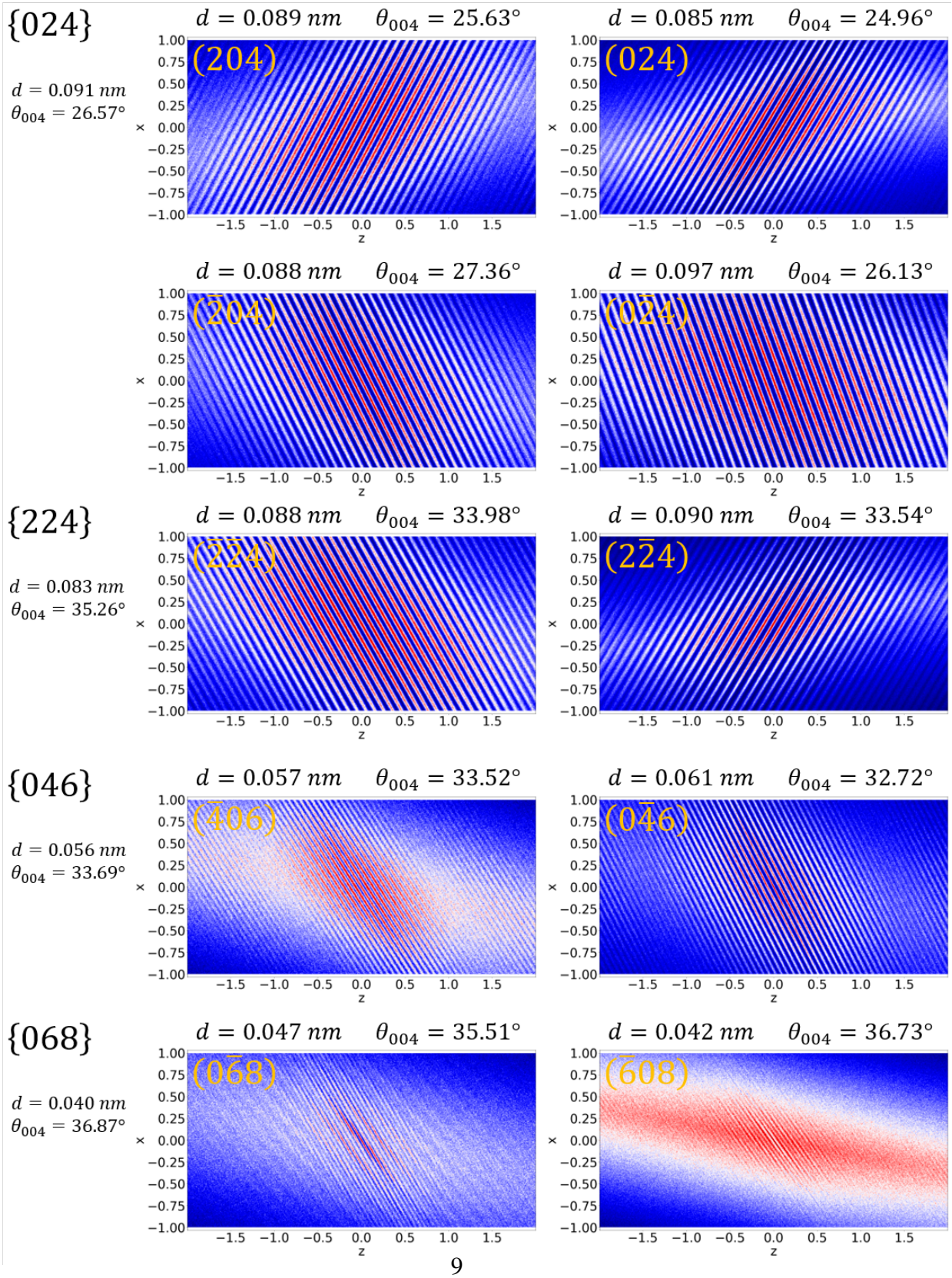
{024}
$d = 0.091\ nm$
$\theta_{004} = 26.57°$
$d = 0.089\ nm$ $\theta_{004} = 25.63°$
(204)
$d = 0.085\ nm$ $\theta_{004} = 24.96°$
(024)
$d = 0.088\ nm$ $\theta_{004} = 27.36°$
($\bar{2}04$)
$d = 0.097\ nm$ $\theta_{004} = 26.13°$
(0$\bar{2}$4)
{224}
$d = 0.083\ nm$
$\theta_{004} = 35.26°$
$d = 0.088\ nm$ $\theta_{004} = 33.98°$
($\bar{2}\bar{2}$4)
$d = 0.090\ nm$ $\theta_{004} = 33.54°$
(2$\bar{2}$4)
{046}
$d = 0.056\ nm$
$\theta_{004} = 33.69°$
$d = 0.057\ nm$ $\theta_{004} = 33.52°$
($\bar{4}$06)
$d = 0.061\ nm$ $\theta_{004} = 32.72°$
(0$\bar{4}$6)
{068}
$d = 0.040\ nm$
$\theta_{004} = 36.87°$
$d = 0.047\ nm$ $\theta_{004} = 35.51°$
(0$\bar{6}$8)
$d = 0.042\ nm$ $\theta_{004} = 36.73°$
($\bar{6}$08)
x
z

{026}

$d = 0.064\ nm$
$\theta_{004} = 18.43°$

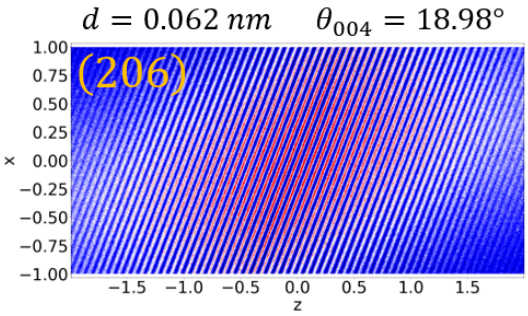

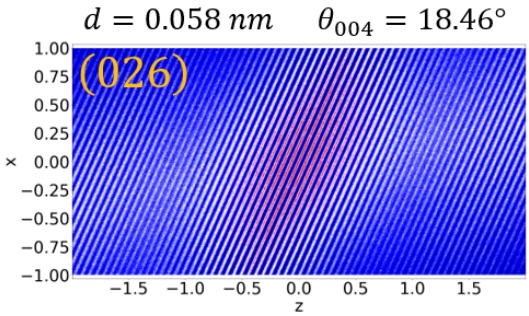

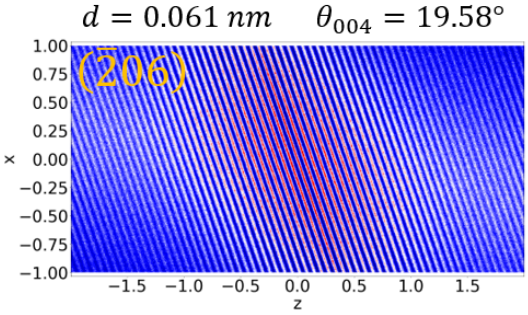

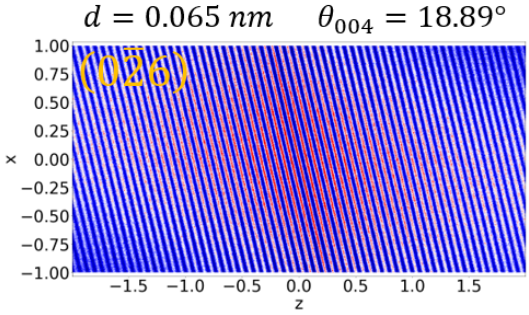

{246}

$d = 0.054\ nm$
$\theta_{004} = 36.70°$

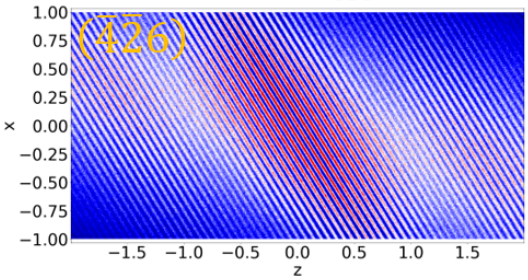

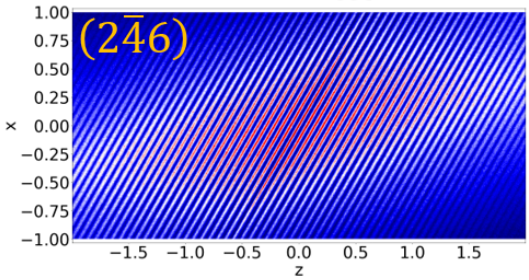

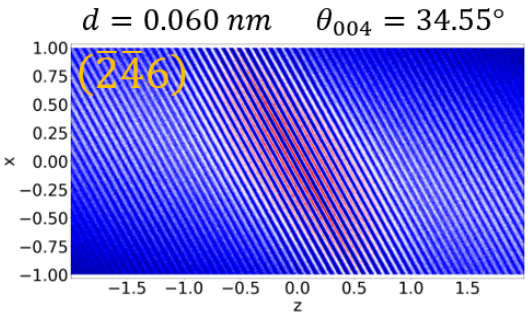

{468}

$d = 0.038\ nm$
$\theta_{004} = 42.03°$

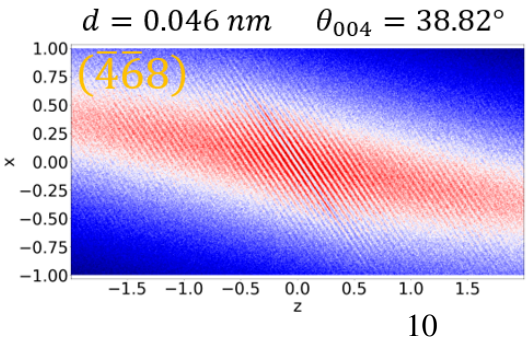

{028}

$d = 0.049\ nm$
$\theta_{004} = 14.04°$

$d = 0.047\ nm$ $\theta_{004} = 14.28°$

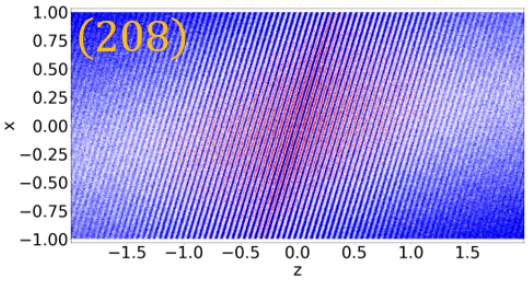

$d = 0.45\ nm$ $\theta_{004} = 13.96°$

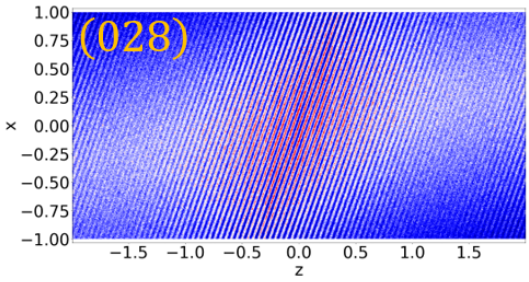

$d = 0.047\ nm$ $\theta_{004} = 14.93°$

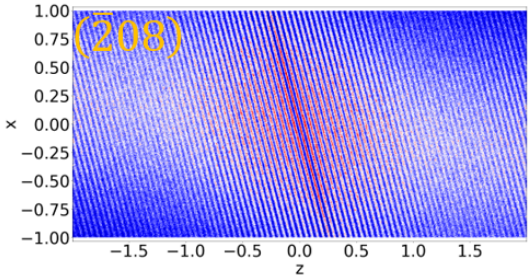

$d = 0.049\ nm$ $\theta_{004} = 14.24°$

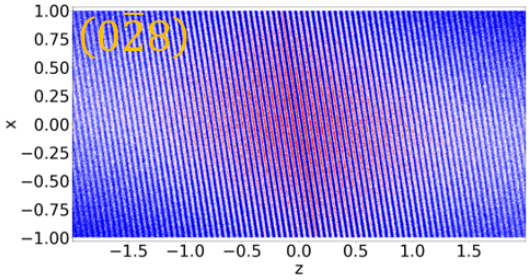

{268}

$d = 0.040\ nm$
$\theta_{004} = 38.33°$

$d = 0.043\ nm$ $\theta_{004} = 37.01°$

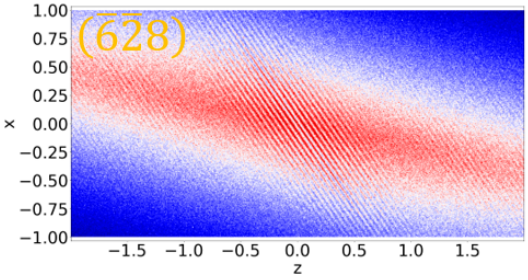

$d = 0.048\ nm$ $\theta_{004} = 36.37°$

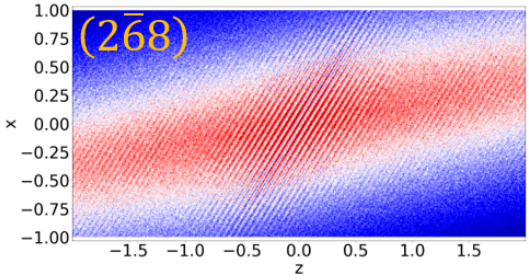

$d = 0.047\ nm$ $\theta_{004} = 36.59°$

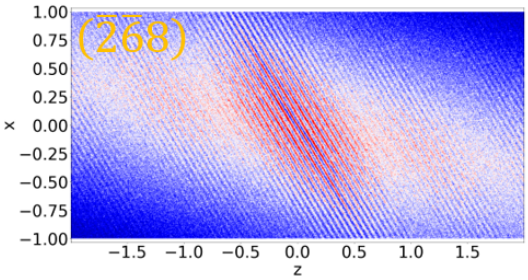

{0 2 10}

$d = 0.040\ nm$
$\theta_{004} = 11.31°$

$d = 0.037\ nm$ $\theta_{004} = 11.57°$

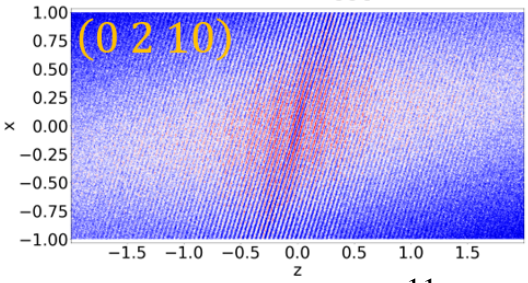

$d = 0.038\ nm$ $\theta_{004} = 11.71°$

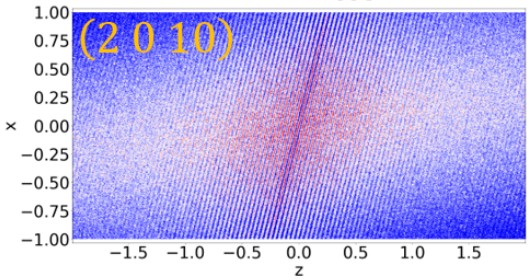

{248}

$d = 0.044\ nm$
$\theta_{004} = 29.21°$

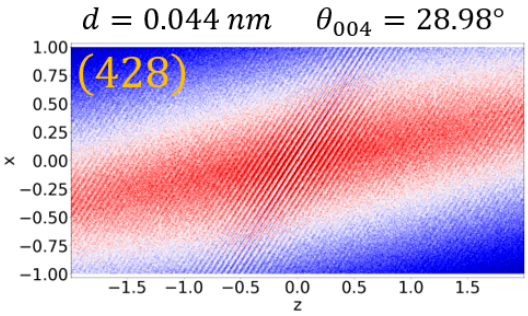

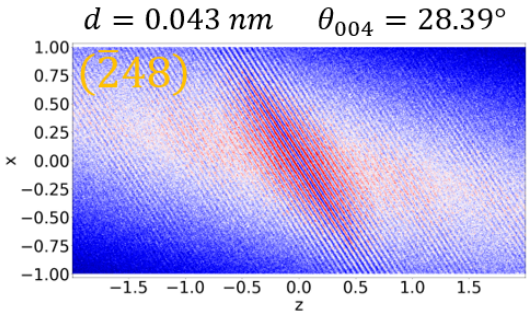

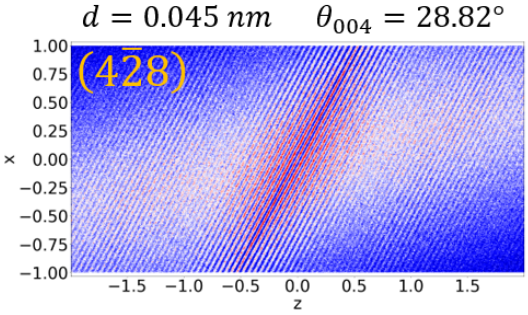

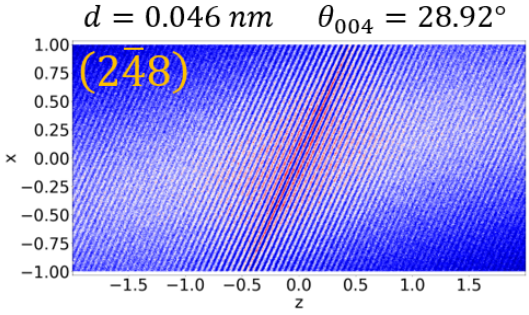

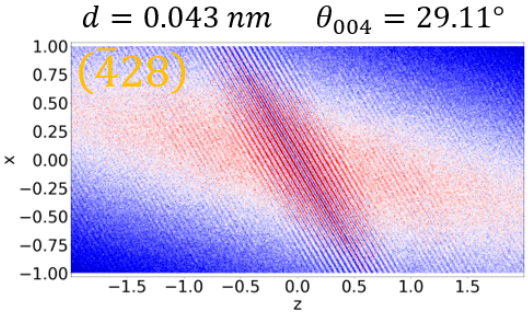

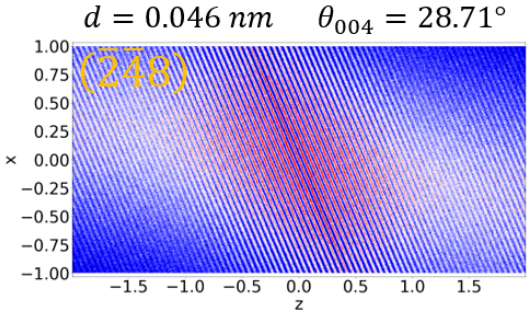

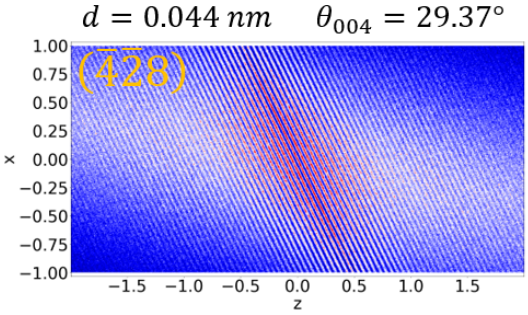

{4 0 10}

$d = 0.038\ nm$
$\theta_{004} = 21.80°$

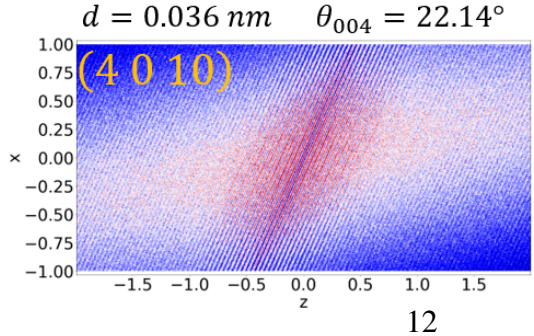

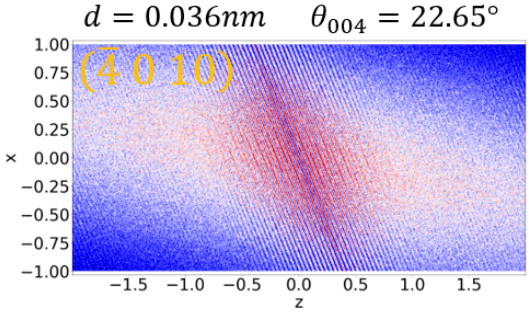

{228}

$d = 0.048\ nm$
$\theta_{004} = 19.47°$

$d = 0.045\ nm$ $\theta_{004} = 19.19°$

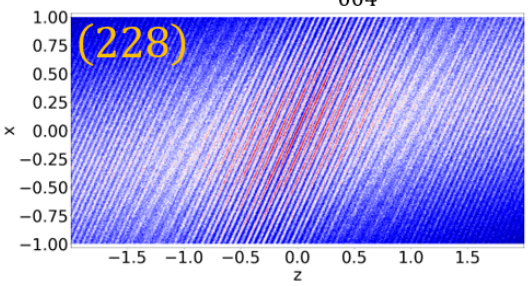

$d = 0.047\ nm$ $\theta_{004} = 19.40°$

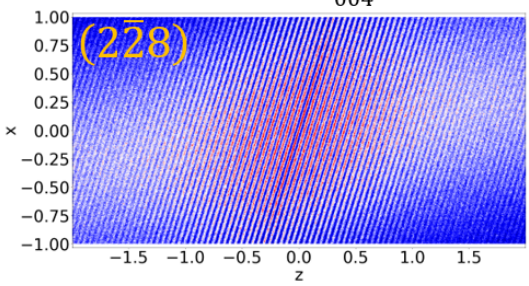

$d = 0.047\ nm$ $\theta_{004} = 19.78°$

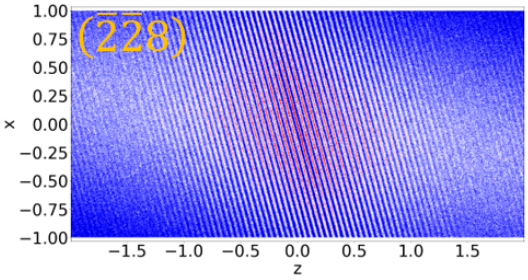

{117}

$d = 0.057\ nm$
$\theta_{004} = 11.42°$

$d = 0.053\ nm$ $\theta_{004} = 11.74°$

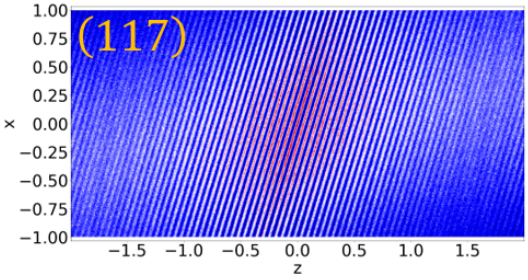

$d = 0.054\ nm$ $\theta_{004} = 12.19°$

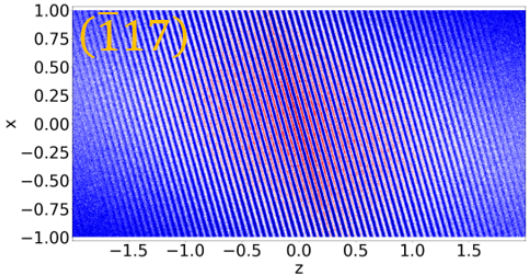

$d = 0.055\ nm$ $\theta_{004} = 12.23°$

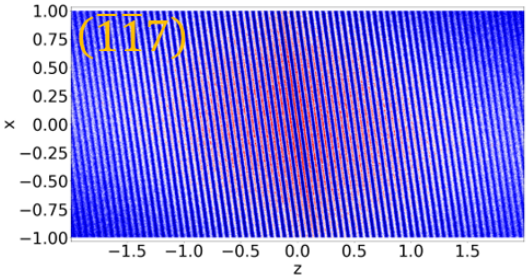

$d = 0.056\ nm$ $\theta_{004} = 11.74°$

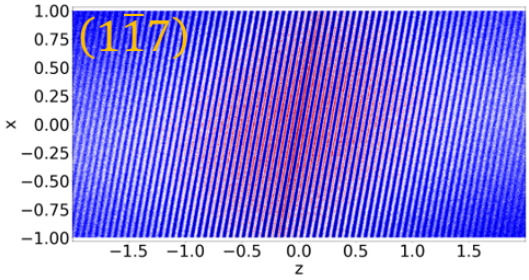

{119}

$d = 0.044\ nm$
$\theta_{004} = 8.93°$

$d = 0.041\ nm$ $\theta_{004} = 9.90°$

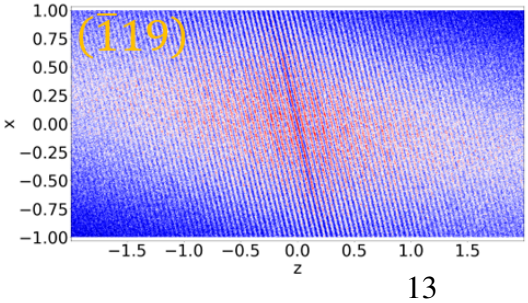

$d = 0.043\ nm$ $\theta_{004} = 9.44°$

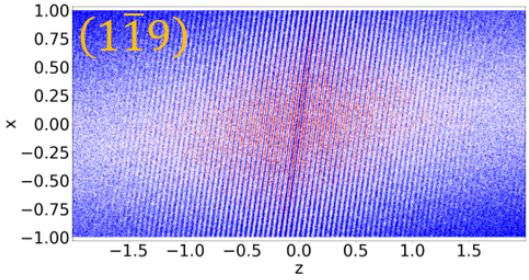

{135}

$d = 0.068\ nm$
$\theta_{004} = 32.31°$

$d = 0.074\ nm$ $\theta_{004} = 31.23°$

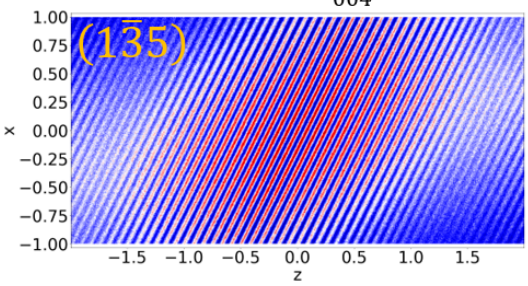

$d = 0.074\ nm$ $\theta_{004} = 31.10°$

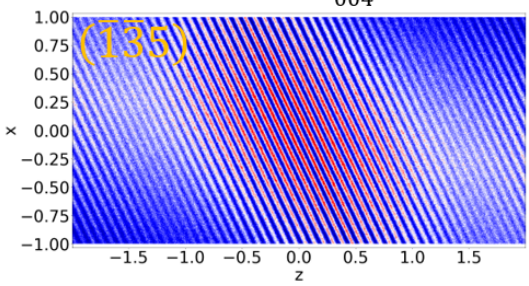

$d = 0.069\ nm$ $\theta_{004} = 31.93°$

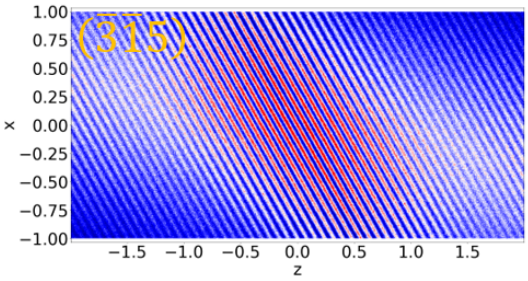

$d = 0.071\ nm$ $\theta_{004} = 31.32°$

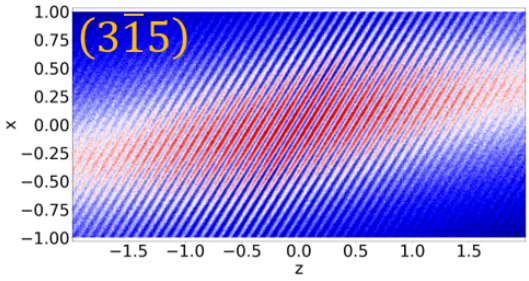

$d = 0.069\ nm$ $\theta_{004} = 31.50°$

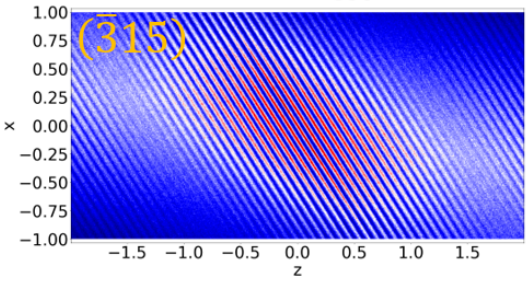

{157}

$d = 0.047\ nm$
$\theta_{004} = 36.07°$

$d = 0.048\ nm$ $\theta_{004} = 35.10°$

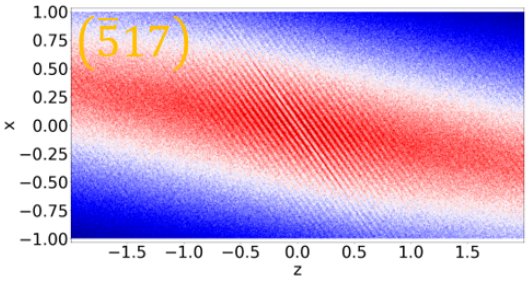

$d = 0.052\ nm$ $\theta_{004} = 34.29°$

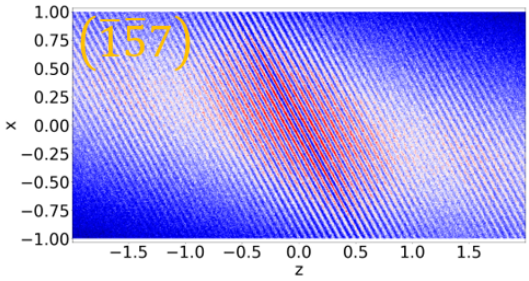

$d = 0.053\ nm$ $\theta_{004} = 34.72°$

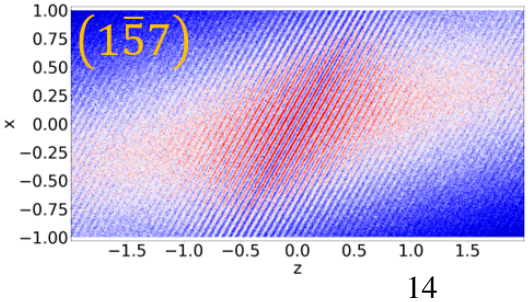

{137}

$d = 0.053\ nm$
$\theta_{004} = 24.31°$

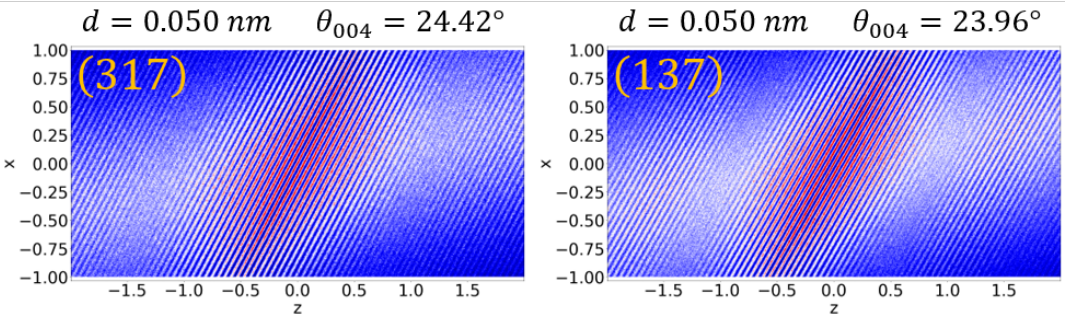

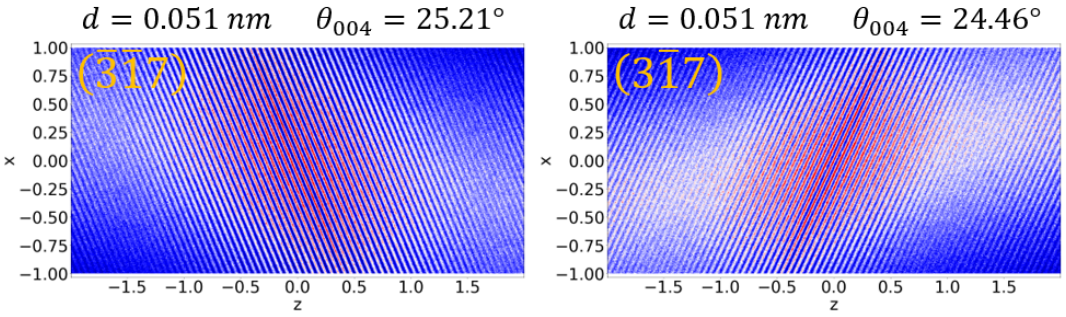

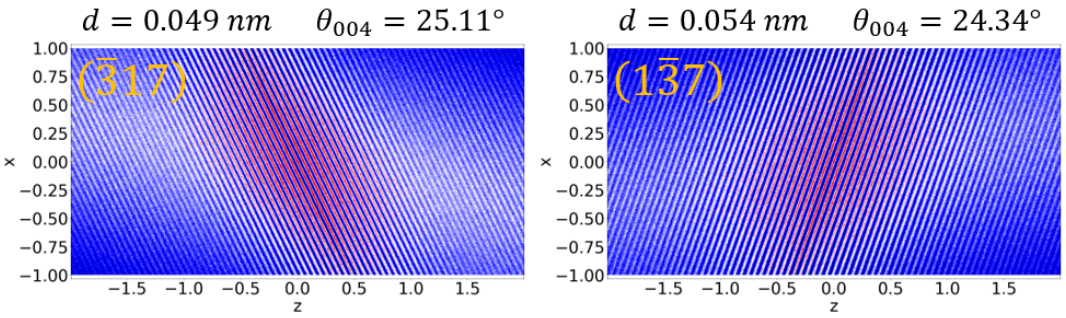

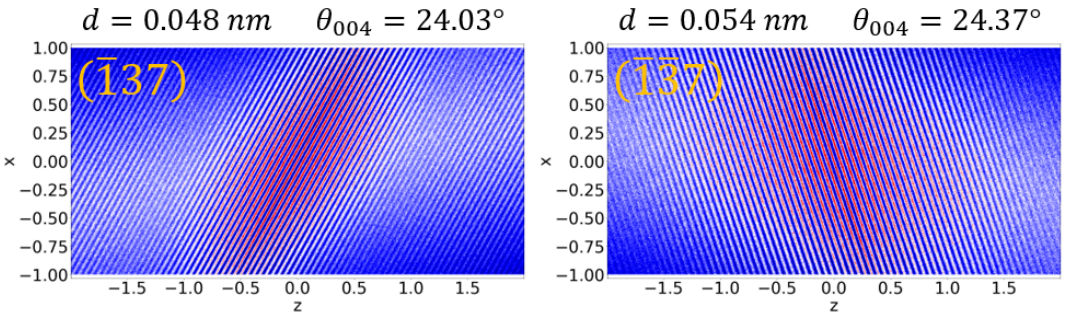

{357}

$d = 0.044\ nm$
$\theta_{004} = 39.79°$

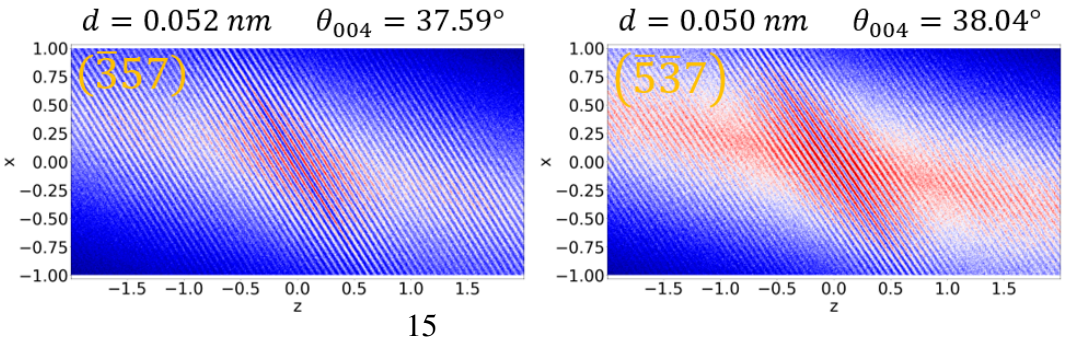

{139}

$d = 0.042\ nm$
$\theta_{004} = 19.36°$

$d = 0.041\ nm$ $\theta_{004} = 19.56°$

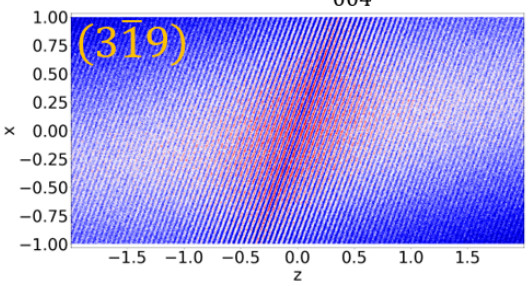

$d = 0.039\ nm$ $\theta_{004} = 19.36°$

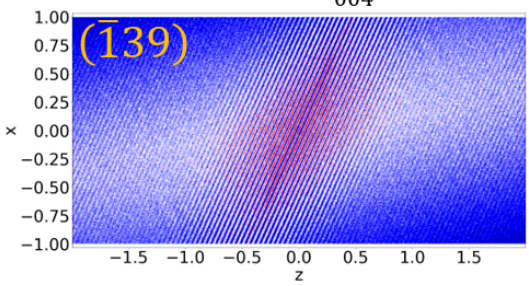

$d = 0.041\ nm$ $\theta_{004} = 20.29°$

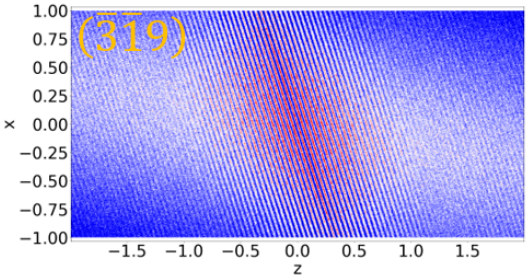

$d = 0.043\ nm$ $\theta_{004} = 19.52°$

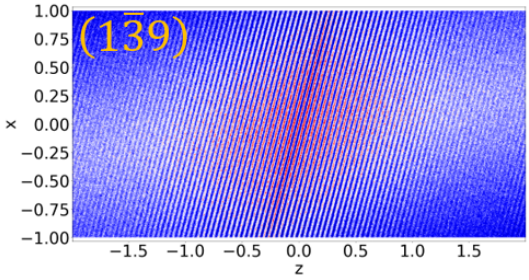

$d = 0.040\ nm$ $\theta_{004} = 19.60°$

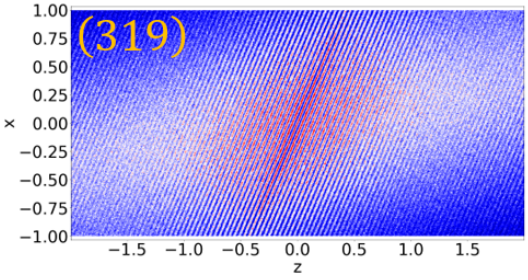

$d = 0.043\ nm$ $\theta_{004} = 19.59°$

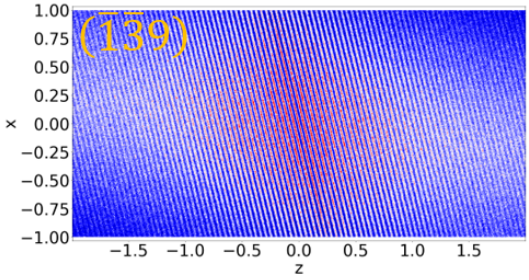

$d = 0.040\ nm$ $\theta_{004} = 20.20°$

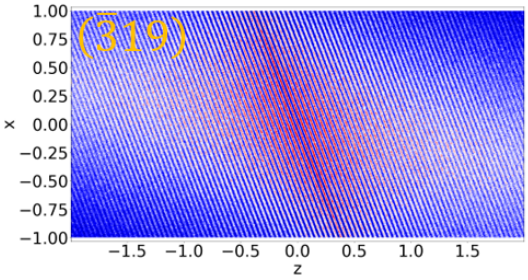

$d = 0.039\ nm$ $\theta_{004} = 19.19°$

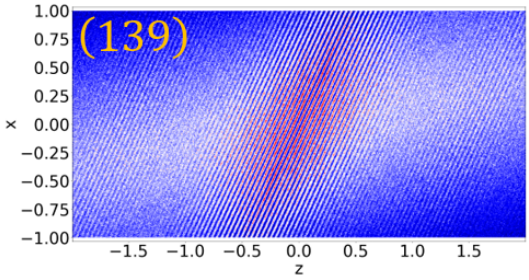

{379}

$d = 0.034\ nm$
$\theta_{004} = 40.24°$

$d = 0.041\ nm$ $\theta_{004} = 38.55°$

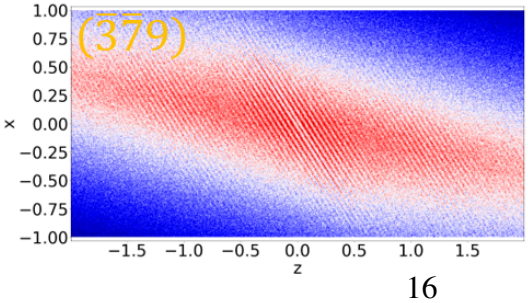

{159}

$d = 0.039\ nm$
$\theta_{004} = 29.53°$

$d = 0.039\ nm$ $\theta_{004} = 28.97°$

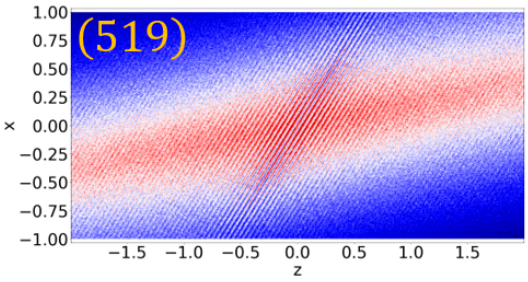

$d = 0.040\ nm$ $\theta_{004} = 28.85°$

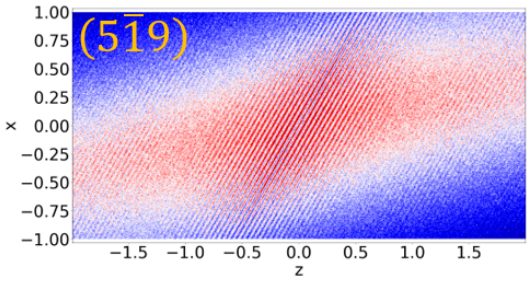

$d = 0.041\ nm$ $\theta_{004} = 28.76°$

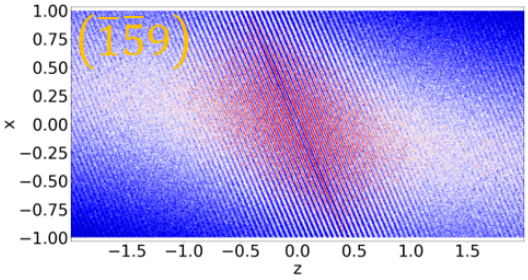

$d = 0.041\ nm$ $\theta_{004} = 28.68°$

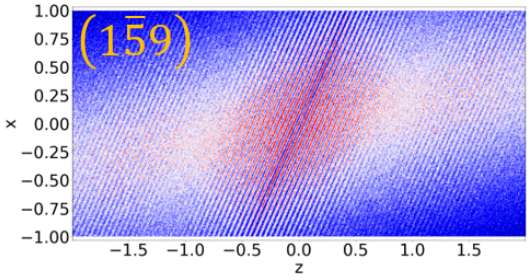

$d = 0.038\ nm$ $\theta_{004} = 29.72°$

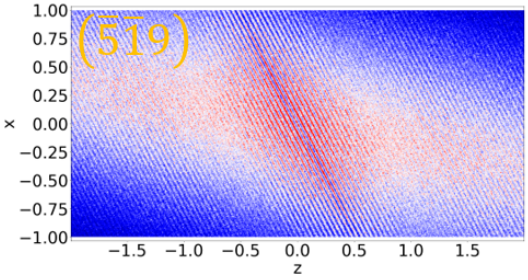

$d = 0.038\ nm$ $\theta_{004} = 29.76°$

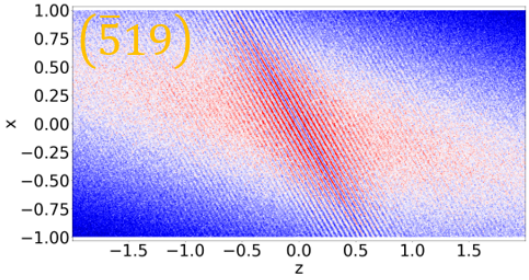

{539}

$d = 0.038\ nm$
$\theta_{004} = 32.94°$

$d = 0.040\ nm$ $\theta_{004} = 32.65°$

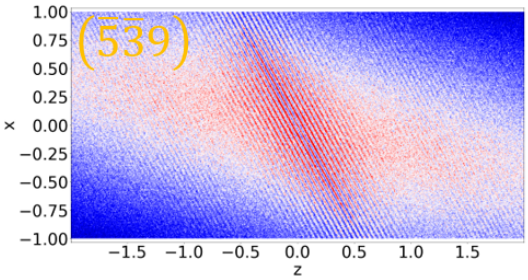

$d = 0.039\ nm$ $\theta_{004} = 32.03°$

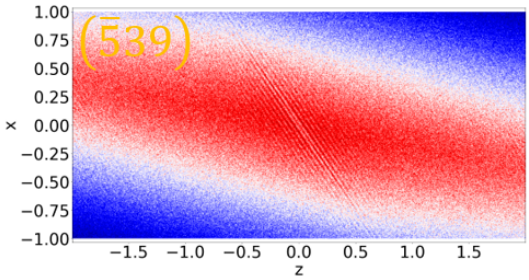

$d = 0.041\ nm$ $\theta_{004} = 32.03°$

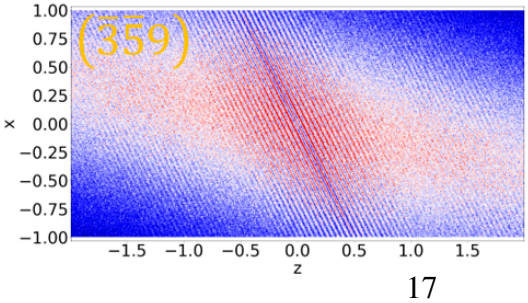

{335}

$d = 0.062\ nm$
$\theta_{004} = 40.32°$

$d = 0.070\ nm$ $\theta_{004} = 38.25°$

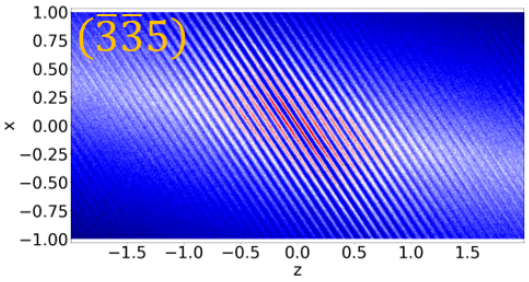

{337}

$d = 0.049\ nm$
$\theta_{004} = 31.22°$

$d = 0.052\ nm$ $\theta_{004} = 30.49°$

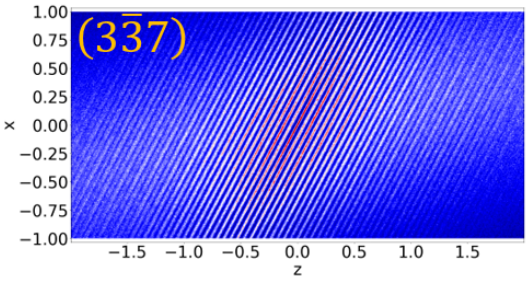

$d = 0.048\ nm$ $\theta_{004} = 30.30°$

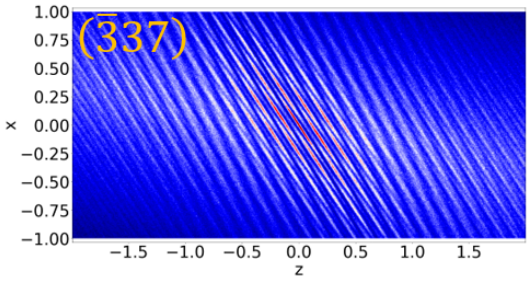

{4 2 10}

$d = 0.037\ nm$
$\theta_{004} = 24.09°$

$d = 0.035\ nm$ $\theta_{004} = 24.83°$

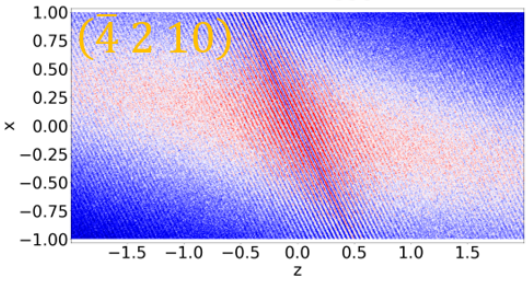

$d = 0.037\ nm$ $\theta_{004} = 24.32°$

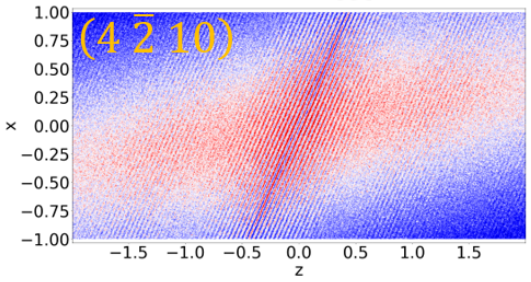

{4 6 10}

$d = 0.033\ nm$
$\theta_{004} = 35.80°$

$d = 0.037\ nm$ $\theta_{004} = 34.00°$

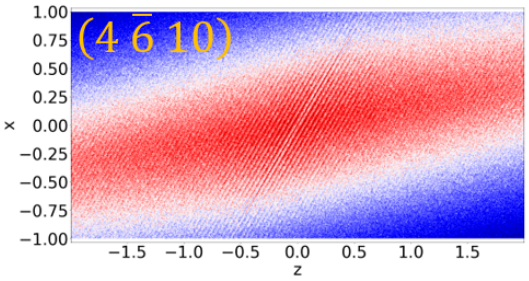

$d = 0.037\ nm$ $\theta_{004} = 34.49°$

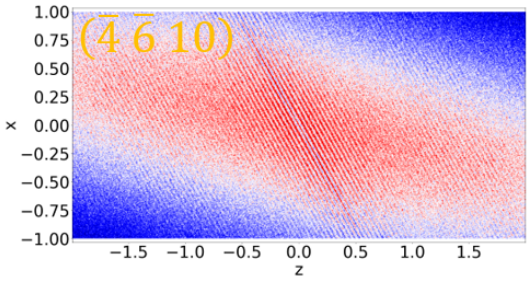

$d = 0.035\ nm$ $\theta_{004} = 34.93°$

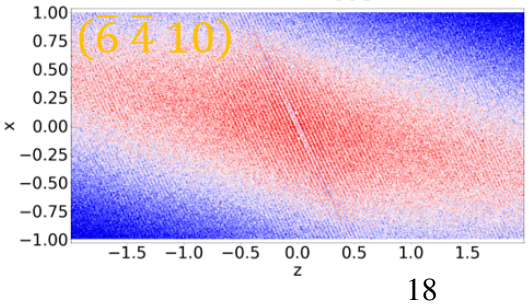

{1 3 11}

$d = 0.035\ nm$
$\theta_{004} = 16.04°$

$d = 0.033\ nm$ $\theta_{004} = 16.08°$

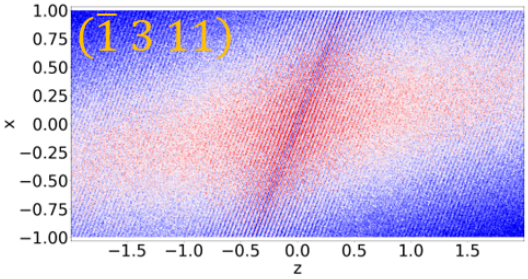

$d = 0.034\ nm$ $\theta_{004} = 16.93°$

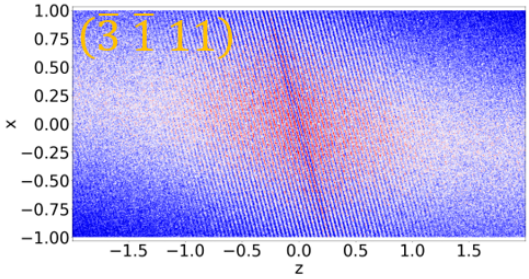

$d = 0.036\ nm$ $\theta_{004} = 16.30°$

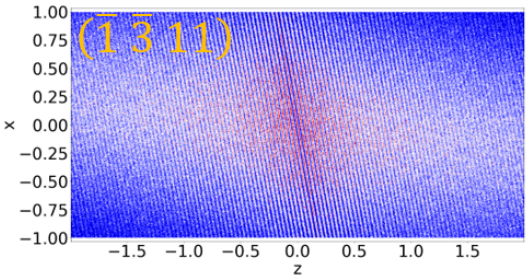

$d = 0.034\ nm$ $\theta_{004} = 16.27°$

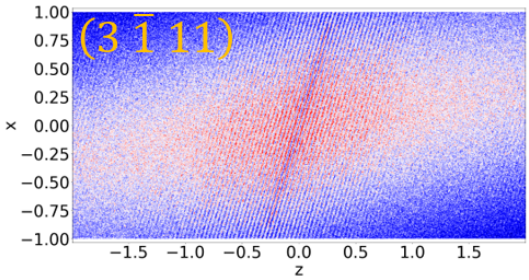

$d = 0.033\ nm$ $\theta_{004} = 15.90°$

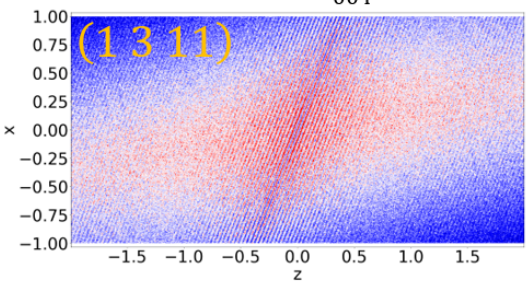

$d = 0.033\ nm$ $\theta_{004} = 16.87°$

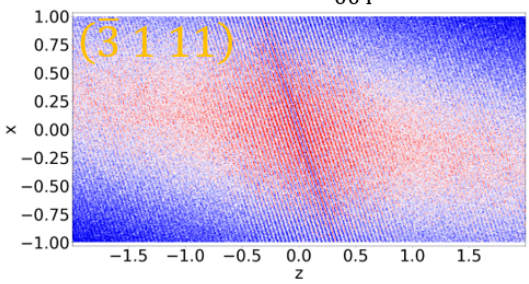

$d = 0.036\ nm$ $\theta_{004} = 16.20°$

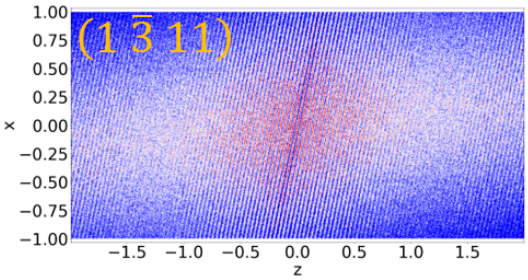

{7 3 11}

$d = 0.030\ nm$
$\theta_{004} = 34.70°$

$d = 0.032\ nm$ $\theta_{004} = 34.85°$

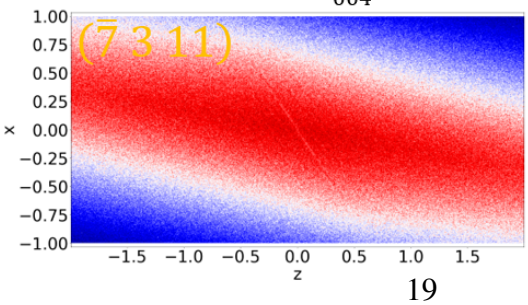

{1 5 11}

$d = 0.033\ nm$
$\theta_{004} = 24.87°$

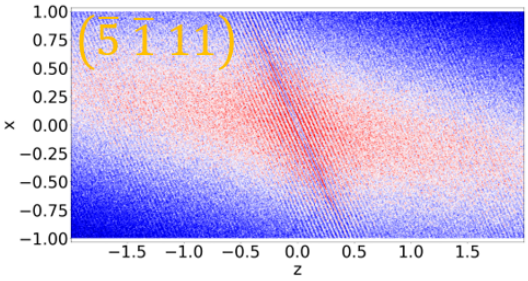

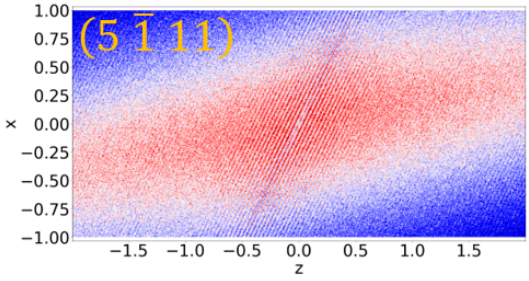

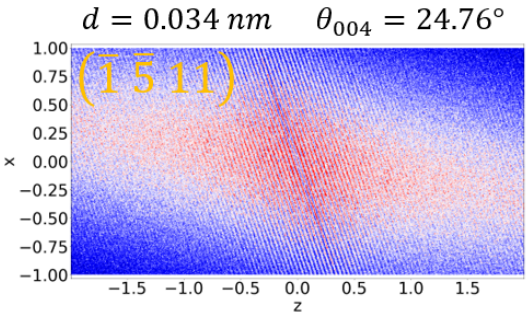

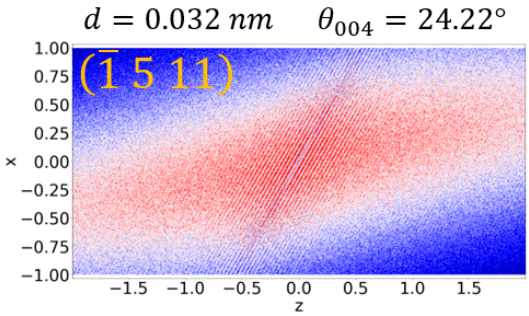

{3 5 11}

$d = 0.033\ nm$
$\theta_{004} = 27.93°$

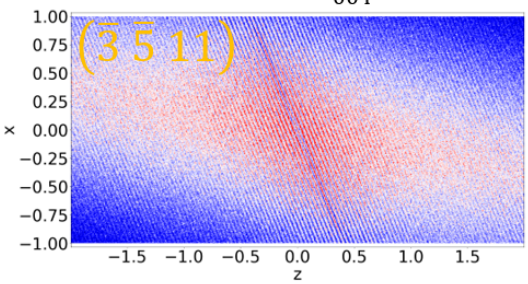

{2 8 10}

$d = 0.031\ nm$
$\theta_{004} = 39.51°$

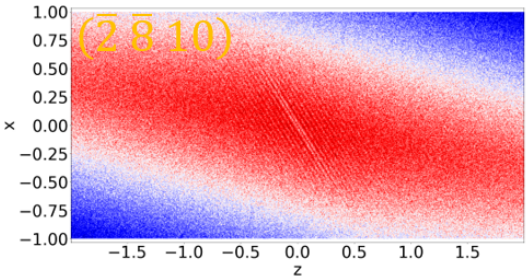

{2 6 12}

$d = 0.030\ nm$
$\theta_{004} = 27.79°$

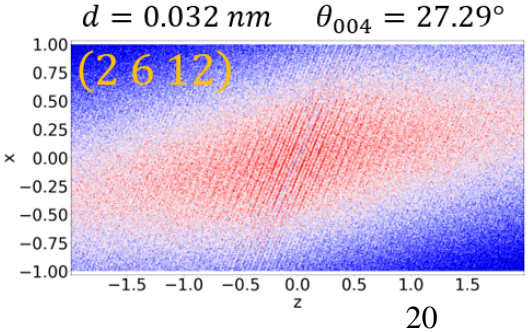

$\{1\ 3\ 13\}$

$d = 0.030\ nm$
$\theta_{004} = 13.67°$

$d = 0.029\ nm$ $\theta_{004} = 14.48°$

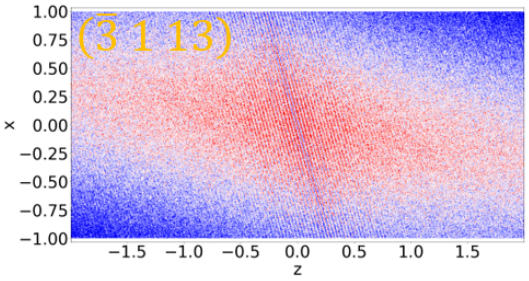

$d = 0.028\ nm$ $\theta_{004} = 13.61°$

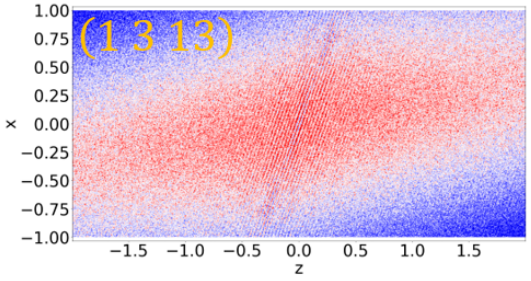

$d = 0.031\ nm$ $\theta_{004} = 14.02°$

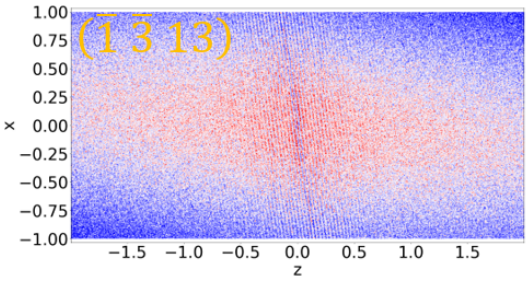

$d = 0.030\ nm$ $\theta_{004} = 13.86°$

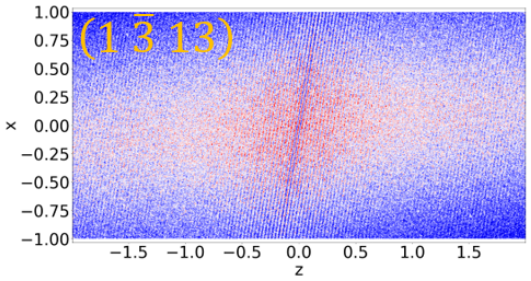

$d = 0.028\ nm$ $\theta_{004} = 13.70°$

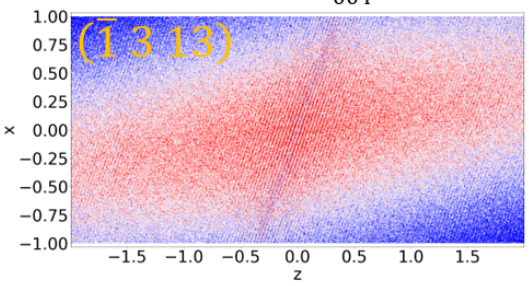

{1 5 13}

$d = 0.029\ nm$
$\theta_{004} = 21.42°$

$d = 0.029\ nm$ $\theta_{004} = 21.48°$

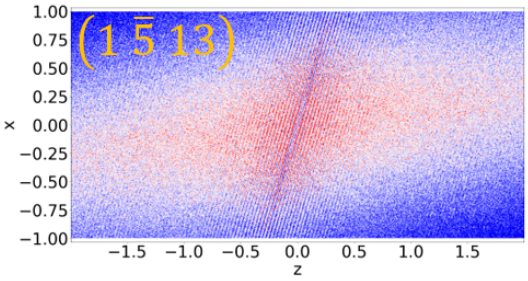

$d = 0.027\ nm$ $\theta_{004} = 21.08°$

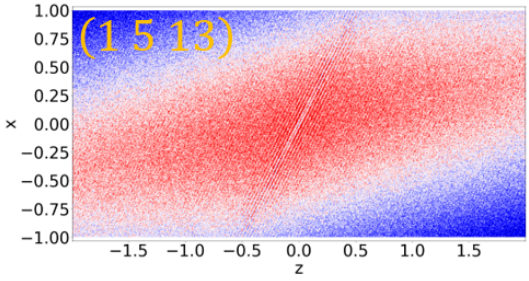

$d = 0.029\ nm$ $\theta_{004} = 22.46°$

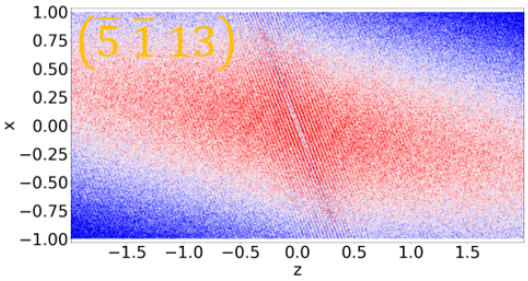

$d = 0.029\ nm$ $\theta_{004} = 21.75°$

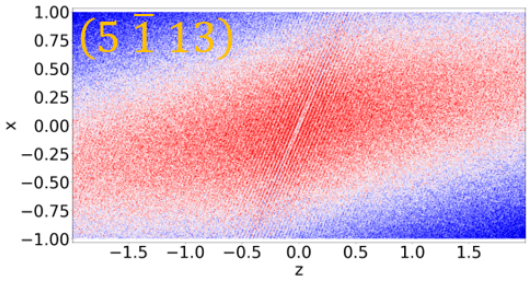

$d = 0.028\ nm$ $\theta_{004} = 22.36°$

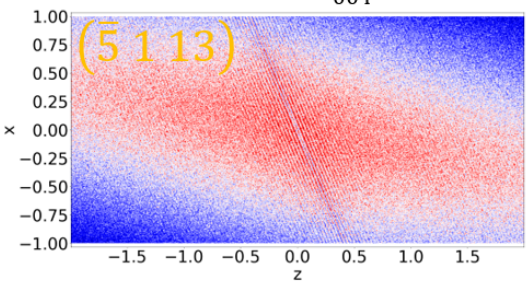

{4 6 12}

$d = 0.029\ nm$
$\theta_{004} = 31.00°$

$d = 0.031\ nm$ $\theta_{004} = 30.47°$

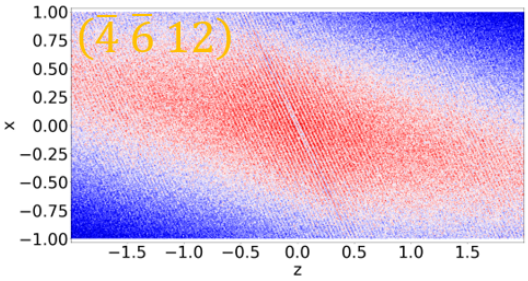

{2 4 14}

$d = 0.028\ nm$
$\theta_{004} = 17.71°$

$d = 0.026\ nm$ $\theta_{004} = 17.44°$

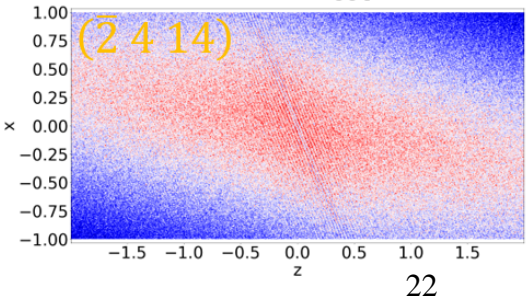

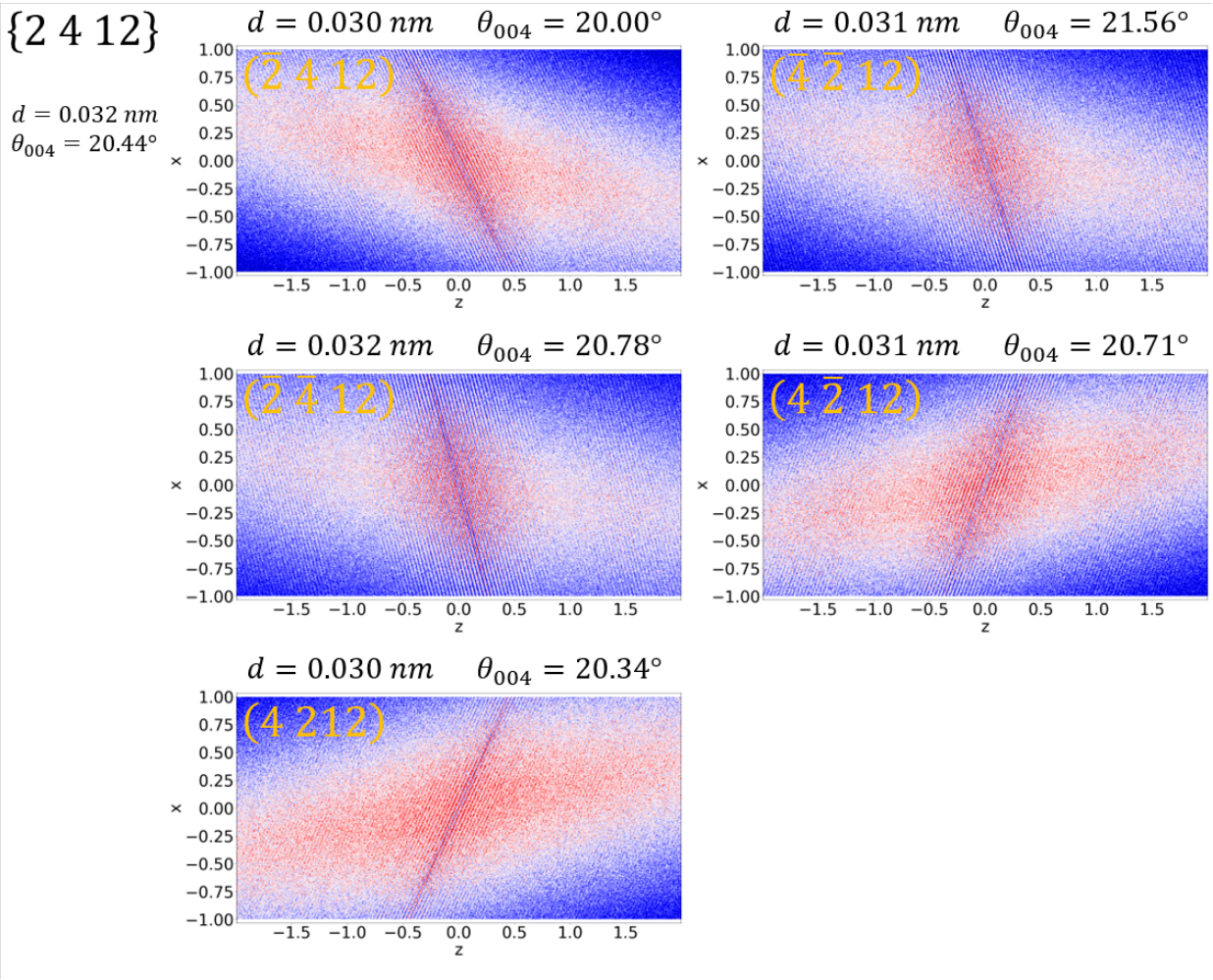

Figure S3: **Spatial distribution maps of plane sets in aluminum:** The left column shows the miller index, the expected plane spacing and the expected angle to the 002 plane set for each set of planes. For each reconstructed plane set the measured angle and plane distance extracted from a direct Fourier analysis (*5*) of the volume containing the planes are noted.

3 Atomic planes imaged in laser pulsed Silicon-Germanium-Tin

The Silicon-Germanium-Tin with 6% Silicon and 4% Tin ($Si_6Ge_{90}Sn_4$) and is run on a LEAP 5000 XS in laser pulse mode with a pulse energy of 10 pJ and a base temperature of 25 K. The full data set is shown in the main manuscript. The filtered data set contains 35e6 ions collected at a voltage between 6.6 and 6.9 kV. We use the procedure described in the section on extracting reconstruction parameters of the main manuscript to reconstruct the data set. This shows that the tip has a starting radius of approximately 88 nm and a cone angle of approximately 1.5°. The 35e6 ions result in the removal of about 118 nm of material.

We use all peaks found by the algorithm and apply the peak search discussed in the previous section. They are shown marked with an 'x' in supplementary fig. S4 overlapped to the FFT signal map and identified with the respective Miller index written in the same color. In addition, the theoretical expected positions of the poles are marked with an 'o'. Overall 4 plane sets were found.

Spatial distribution maps (SDMs) (*4*) for all 4 plane sets are shown in supplementary fig. S5. Plane sets and their properties have been extracted from the volumes in the same way as in section S2.

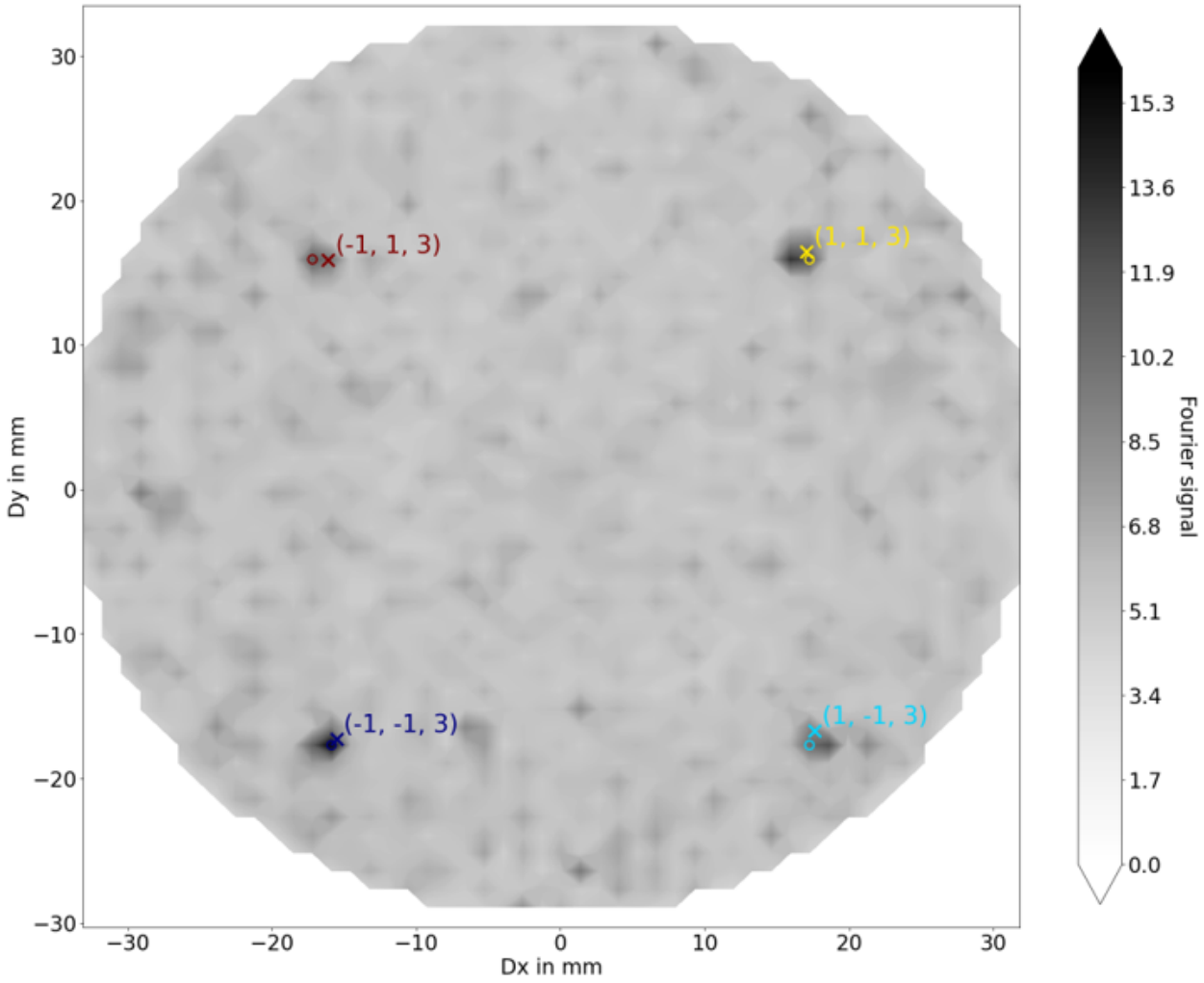

Figure S4: **Pole map of $Si_6Ge_{90}Sn_4$:**. 4 plane sets detected by the algorithm marked with an 'x' and identified by their Miller indices. The theoretical position of the respective poles on a hemisphere are marked with an 'o'. Spatial distribution maps for all 4 plane sets are shown in supplementary fig. S5

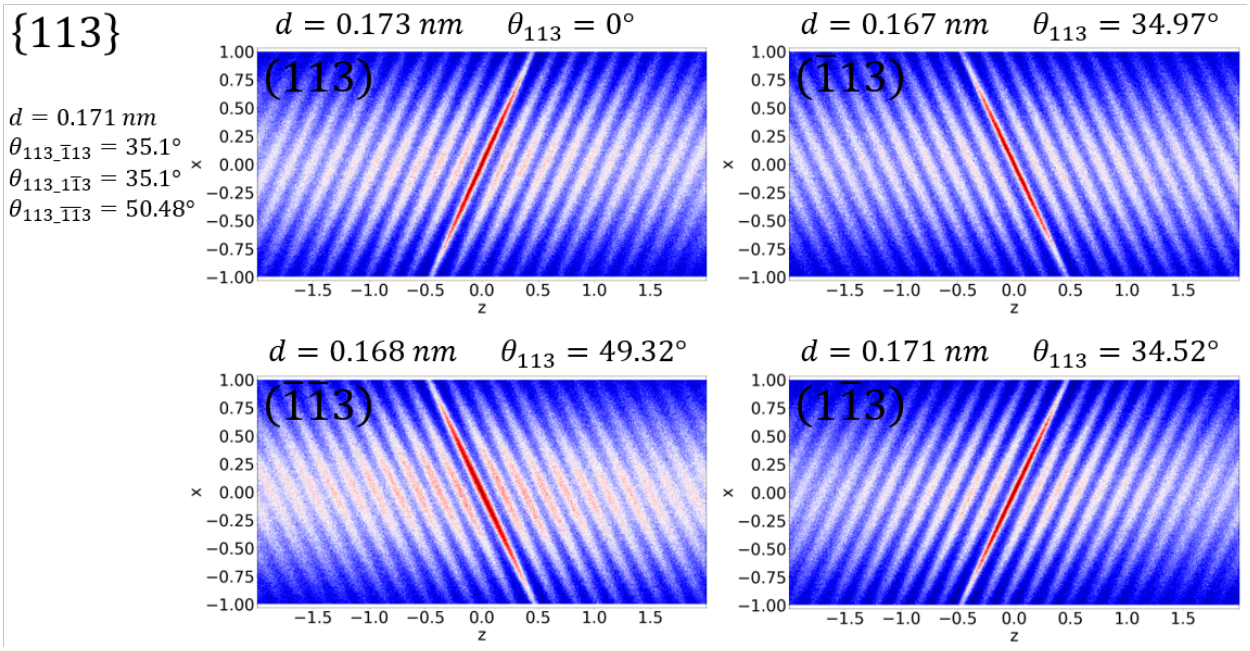

Figure S5: **Spatial distribution maps of plane sets in $Si_6Ge_{90}Sn_4$:** The measured angle and plane distances extracted from a direct Fourier analysis (*5*) of the volume containing the planes are noted.

4 Atomic planes imaged in laser pulsed Silicon

Silicon tips were prepared from a 4 inch nominally intrinsic wafer and measured on a Cameca Invizo 6000 in laser pulse mode with a pulse energy of approxmiatly 50 pJ keeping the ratio of double charged to single charged silicon ions at 80 and the base temperature at 25 K. The filtered data set contains 26e6 ions collected at a voltage between 9.2 and 10.2 kV. We use the procedure described in the section on extracting reconstruction parameters of the main manuscript to reconstruct the data set. This shows that the tip has a starting radius of approximately 65 nm and a cone angle of approximately 4.3°. The 26e6 ions result in the removal of about 58 nm of material.

We use all peaks found by the algorithm and apply the peak search discussed in the previous section. They are shown marked with an 'o' in supplementary fig. S6 overlapped to the FFT signal map and identified with the respective Miller index written in the same color. Overall 8 plane sets were found.

Spatial distribution maps (SDMs) (*4*) for all 8 plane sets are shown in supplementary fig. S7. Plane sets and their properties have been extracted from the volumes in the same way as in section S2.

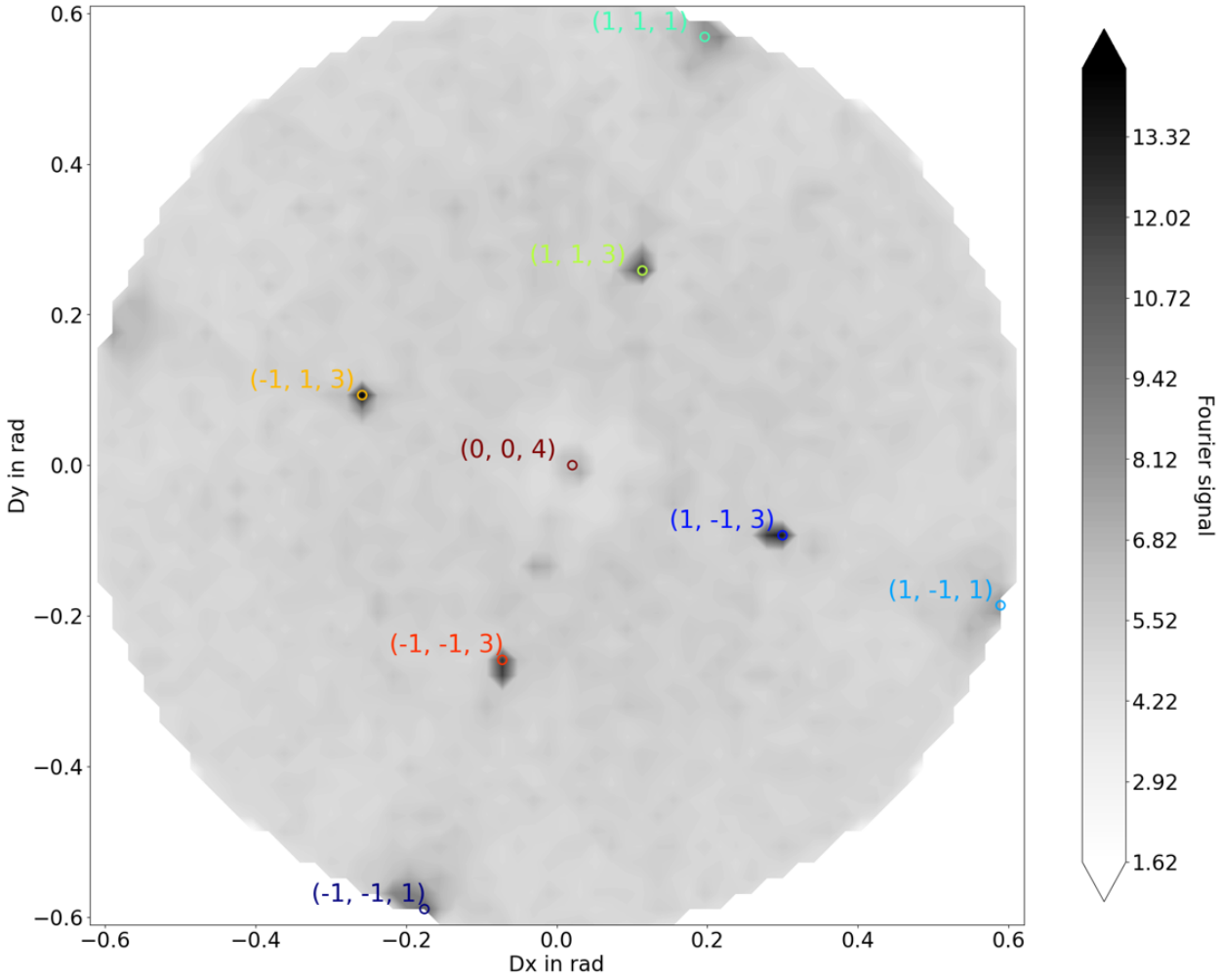

Figure S6: **Pole map of Silicon:** 8 plane sets detected by the algorithm marked with an '0' and identified by their Miller indices. Spatial distribution maps for all 4 plane sets are shown in supplementary fig. S7. Note that the Invizo 6000 utilizes ion optics to enhance the field of view. This enables imaging of additional poles - in particular the $\{111\}$ poles. It is necessary to account for the effect of the ion optics though when utilizing the detector data. The detector coordinates on the plot are given in radians (angle space) after accounting for the ion optics.

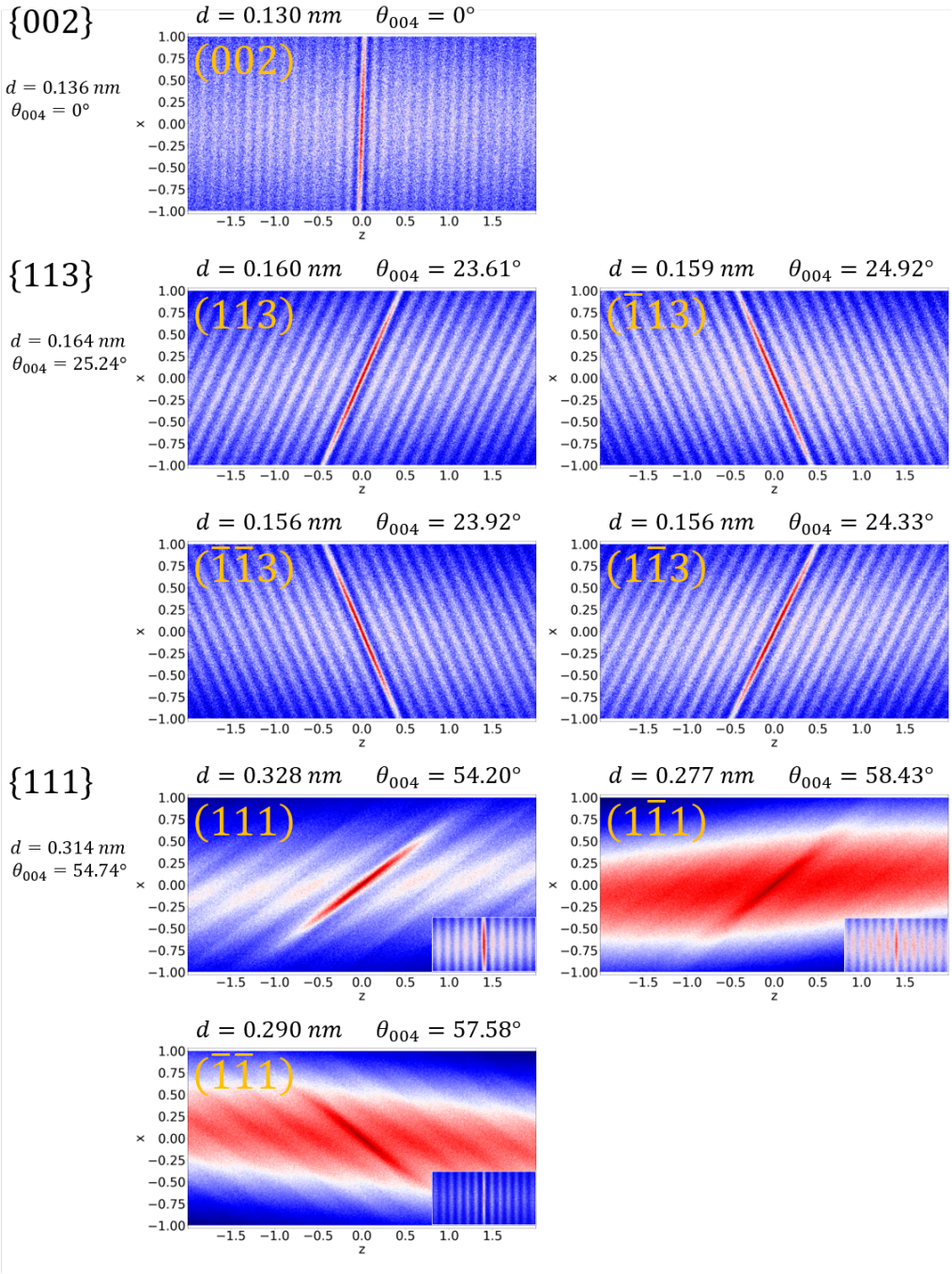

Figure S7: **Spatial distribution maps of plane sets in Silicon:** The measured angle and plane distances extracted from a direct Fourier analysis (*5*) of the volume containing the planes are noted. For the family of {111} planes inlets show the spatial distribution maps for reconstruction perpendicular to the surface similar to Fig. 2 of the main manuscript.

5 The relationship between angle compression and point projection

The projection from the tip surface to the detector in APT is usually modeled as a point projection (*3*) with a projection parameter *m* or a projection under angular compression (*2, 6*) using an image compression factor *ICF*.

For small angles a simple relation between the two parameters can be derived $ICF \approx m+1$ (*2*) Appendix C. The precise relation for two poles on opposite sides of the main axis of the tip with the same angle (e.g. the $(1\ 1\ 3)$ and $(\overline{1}\ \overline{1}\ 3)$ poles on a tip with a diamond lattice oriented along the $(0\ 0\ 4)$ direction) is derived in supplementary Fig. S8.

The relationship is graphed in supplementary Fig. S9. In supplementary Fig. S9a for the geometry discussed in supplementary Fig. S8 and in supplementary Fig. S9b for the a geometry were one pole at an angle of $25.24°$ (e.g. the $(1\ 1\ 3)$ on a $(0\ 0\ 4)$ silicon tip) is fixed and the angle is evaluated between this pole and another pole that is in the same plane with the main axis of the tip (e.g. $(1\ 1\ 5)$, $(1\ 1\ 7)$, $(0\ 0\ 4)$, $(\overline{1}\ \overline{1}\ 5)$ $(\overline{1}\ \overline{1}\ 7)$, $(\overline{1}\ \overline{1}\ 3)$).

The graphs show for a given *ICF* what the *m + 1* parameter evaluates to given the angle between 2 poles in the appropriate geometry. For example the angle between the $(1\ 1\ 3)$ and $(\overline{1}\ \overline{1}\ 3)$ pole in a diamond lattice like Silicon or Germanium is $\alpha_1 = 50.48°$ and the geometry is covered by supplementary Fig. S9a. Utilizing the graphs we can see that if the *ICF* between those 2 poles evaluates to 1.6 than *m + 1* would evaluate to 1.606 and hence *m* to 0.606.

In a similar fashion utilizing supplementary Fig. S9b we can see that if the *ICF* between the $(1\ 1\ 3)$ and the $(\overline{1}\ \overline{1}\ 5)$ evaluates to 1.5 than the corresponding *m + 1* would be 1.504 as the angle between the 2 poles is $\alpha_1 = 41.03°$.

For larger angles the discrepancy between the 2 parameters is more notable. The angle between the $(1\ 1\ 1)$ and $(\overline{1}\ \overline{1}\ 1)$ pole in a diamond lattice is $\alpha_1 = 109.47°$ and hence a *ICF* of

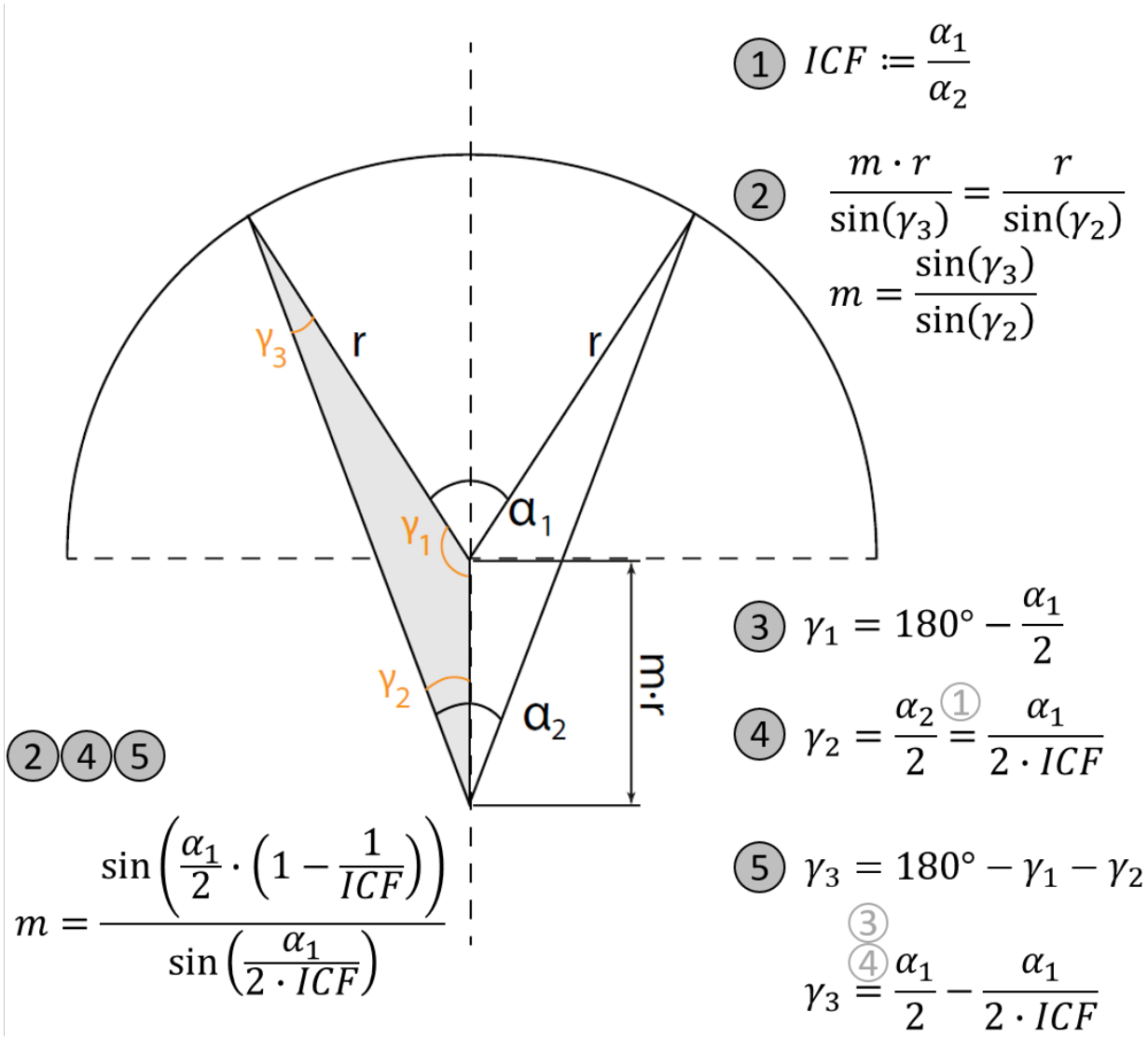

Figure S8: **Relationship between *m* and *ICF***: Note that this derivation only works if the 2 poles that form the angle α_1 on the tip surface are in one plane with the main axis of the tip shaped sample and both have angle $\frac{\alpha_1}{2}$ to the main axis of the tip.

1.6 would correspond to an *m + 1* of 1.624.

Note, that the field of view on a LEAP 5000 XS as used in this work is about $55°$ and hence the difference between *ICF* and *m + 1* is alway less than 0.01.

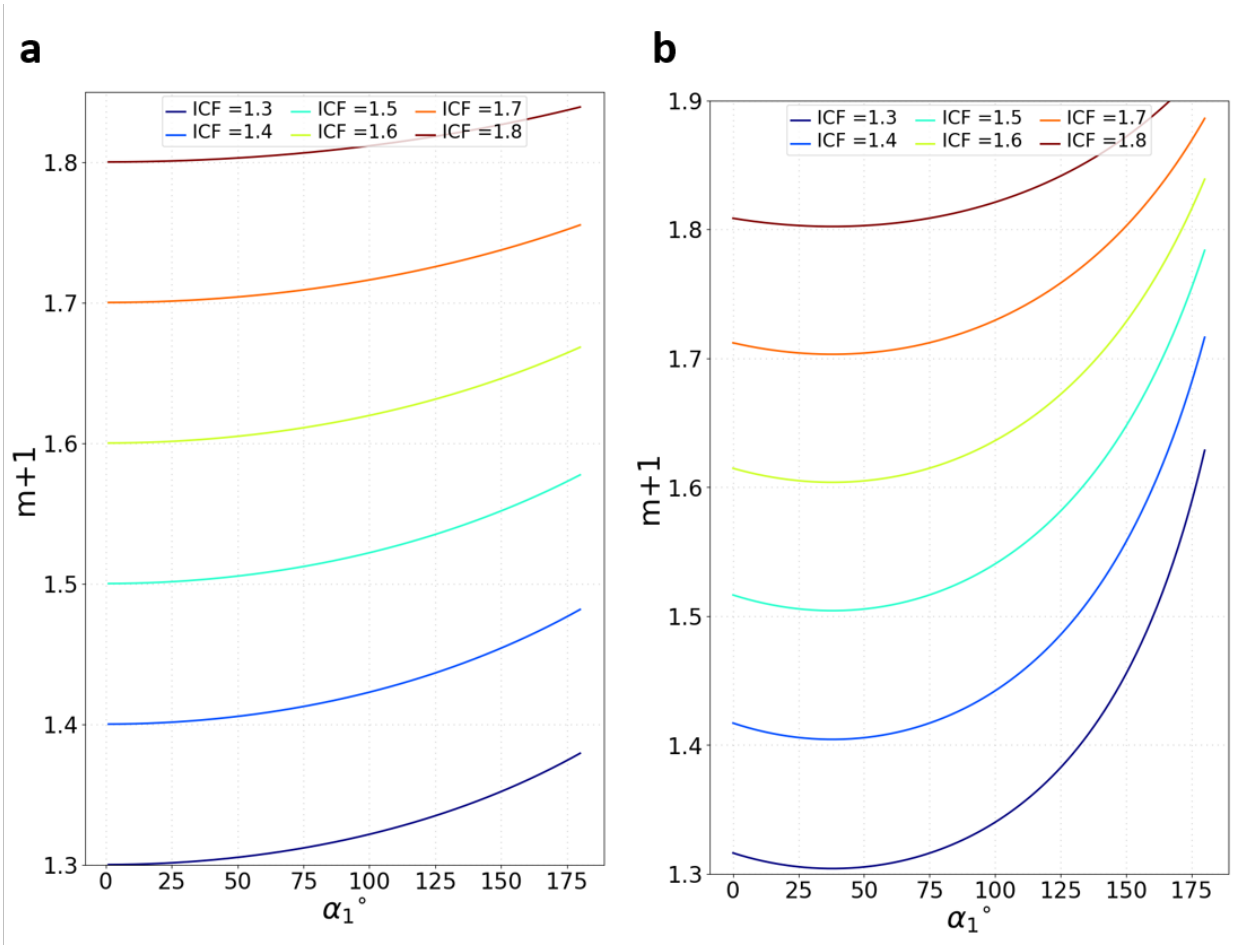

Figure S9: **Relationship between *m* and *ICF***: For the case of 2 poles symmetric to the main axis of the pole with an angle α_1 between the 2 poles (a) and the case between a pole at $25.24°$ off the main axis and a pole in the same plane (b) at an angle α_1 from the first pole. See text for further explanation.

6 Automated extraction of reconstruction parameters from crystal plane data

This section contains additional details to show how the signals of the plane set remnants are used to automatically extract the parameters needed for a dynamic reconstruction (*7*) shown in Fig. 3.

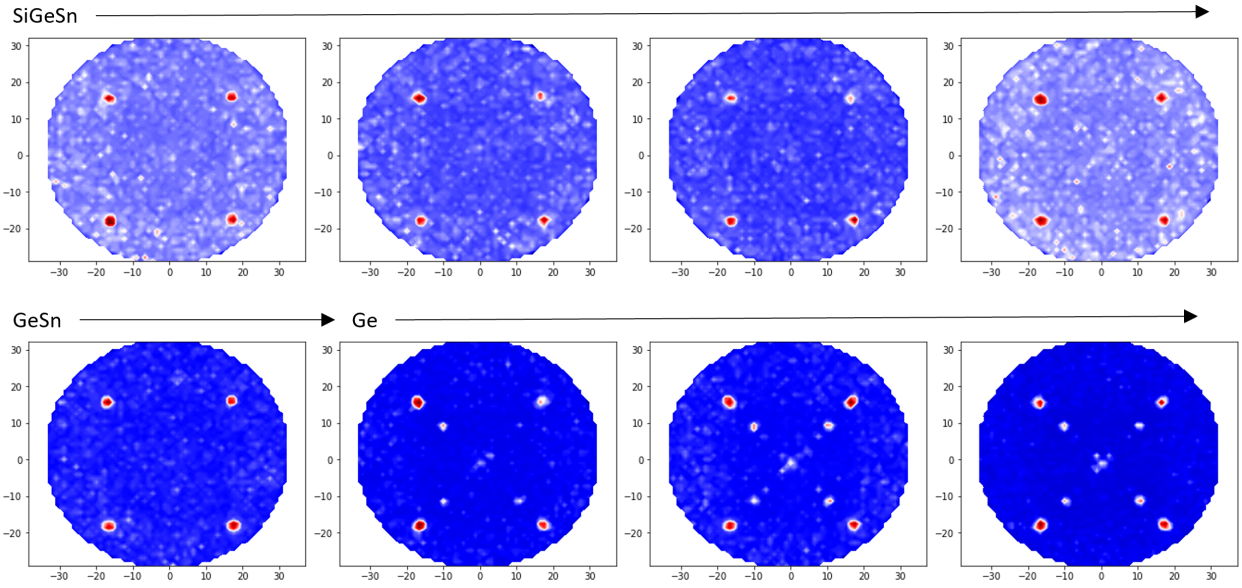

Figure S10: **Series of signal map slices:** each slice contains 5e6 ions corresponding to about 15 nm in depth progression. Blue is low signal. Red is high signal. The x and y axis correspond to the detector of the LEAP 5000 XS. Based on a peak search (*1*) the high signal regions indicating the presence of atomic planes can be identified on each map and hence the respective planes position can be tracked through each depth region.

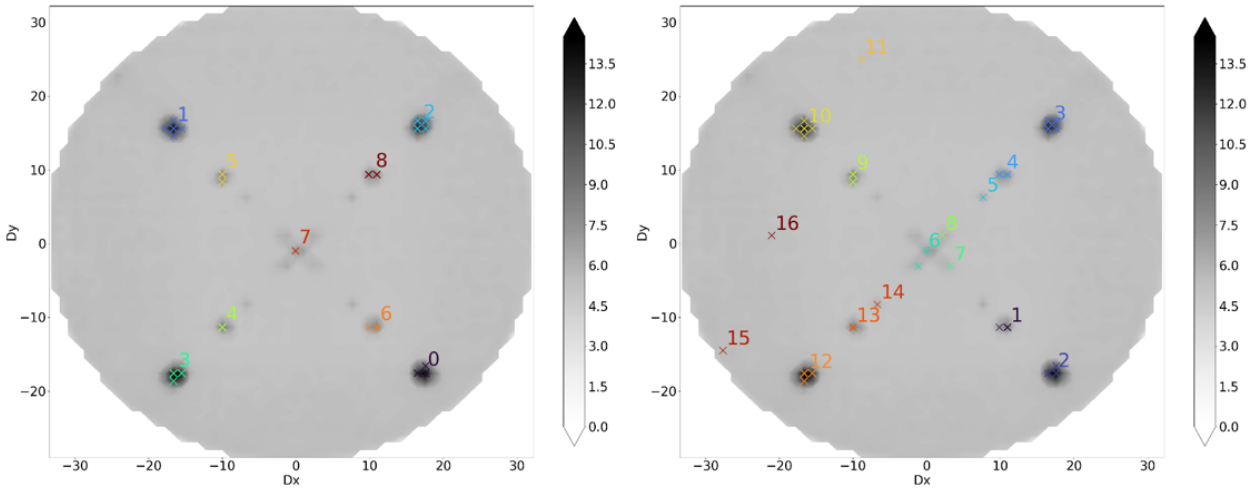

Figure S11: **Clustering the detected plane sets:**. The maps shown in Fig. S8 are processed using a topological peak search (*1*) and can then be clustered such that each cluster represents one plane sets extending through the entire APT measurement or a significant part of it. On the left we show a set of clusters of the mapped plane sets generated by scikit-learn's DBSCAN (*8*) and on the right clusters generated by SciPy's hierarchical linkage (HL) (*9*). Each cluster can now be assigned to the corresponding plane set. We find that clustering with DBSCAN is notably less likely to create false clusters than HL but is more likely to miss smaller clusters as the ones related to the two $\{117\}$ plane sets in this example. After the clustering step, each cluster can be associated to an atomic plane set as shown in Fig. 3 of the main manuscript.

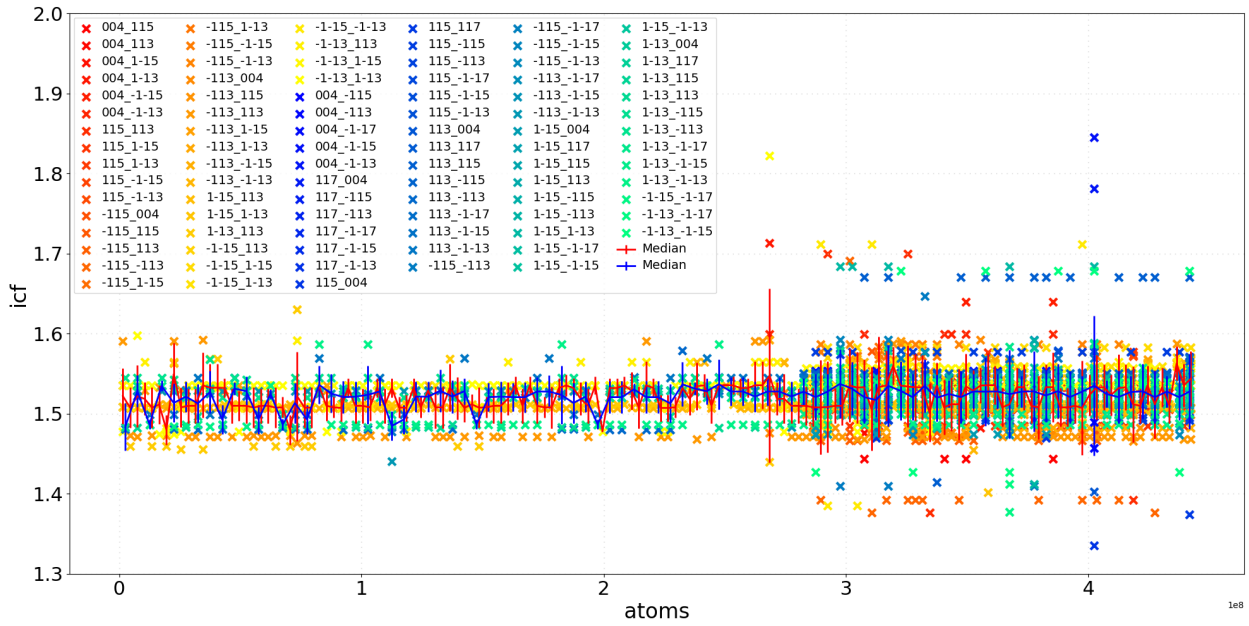

Figure S12: **ICF values from all pairs of identified planes:** For each pair of planes found in any given depth slice, an ICF can be calculated by dividing the known angle between the plane sets (*10*) by the angle formed between the tip and the position of the two plane sets on the detector. The analysis has been done twice for slices of 3e6 ions (red and yellow) and 5e6 ions (blue and green). Collective outliers are caused by the aberration of the tip shaped from the assumed hemispherical shape (*11*), (*3*). Note, that the median ICF is almost identical for both the 3e6 and 5e6 ion slices and does not change notably over the progression of the analysis for this 1.7 μm thick stack of SiGeSn/GeSn/Ge.

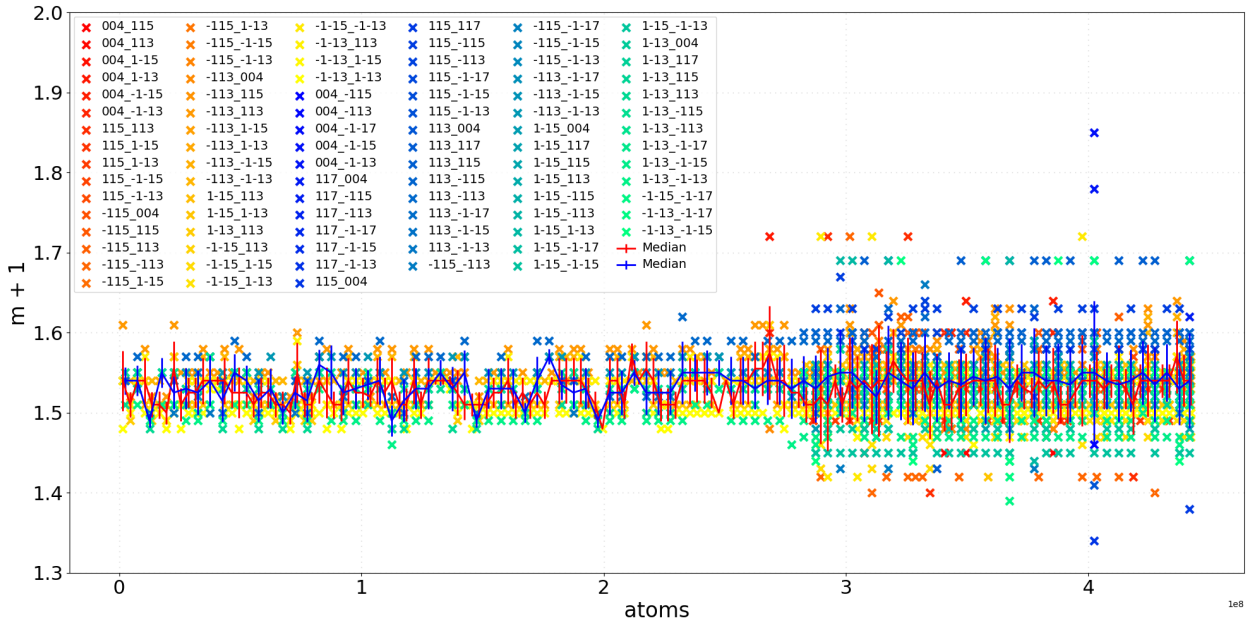

Figure S13: **m + 1 values from all pairs of identified planes:** For each pair of planes found in any given depth slice, the m + 1 parameter is derived using the relationship between ICF and m + 1 discussed in supplementary section S1.

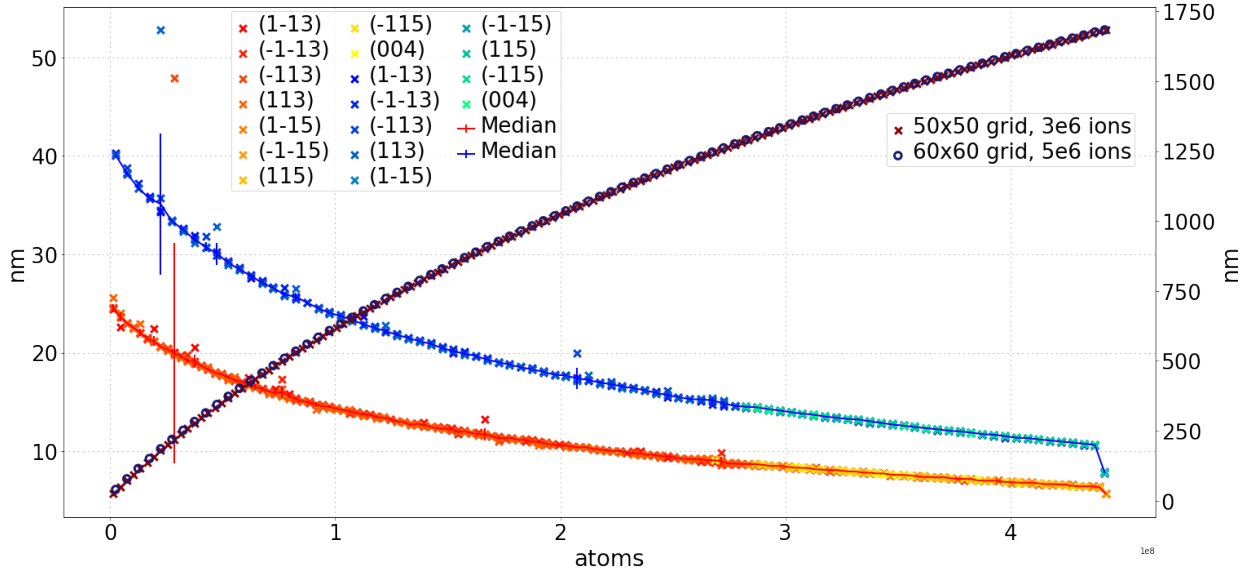

Figure S14: **Depth progression throughout an APT analysis calculated for all identified planes:** From each crystal plane identified in the plane search algorithm a independent estimation of the depth progression can be calculated for each depth slice. We have calculated the progression for both slices of 3e6 (red and yellow) and 5e6 ions (blue and green). In addition the cumulative sum for the median depth progression for both slice sizes is shown in the right y-axis. In effect we measure the distance between planes for each set in a "dummy reconstruction" of known length using the FFT and then scale that length to assure that the distance between planes for the respective plane corresponds to the known distance (*10*). With the exception of a few outliers usually caused by issues with the peak identification in FFT space, this process results in depth estimates for all plane sets that are consistent to within 1%.

References and Notes

1. N. Otter, M. A. Porter, U. Tillmann, P. Grindrod, H. A. Harrington, *EPJ Data Science* **6**, 1 (2017).

2. D. J. Larson, T. Prosa, R. M. Ulfig, B. P. Geiser, T. F. Kelly, *Local electrode atom probe tomography* (Springer, 2013).

3. P. Bas, A. Bostel, B. Deconihout, D. Blavette, *Applied Surface Science* **87**, 298 (1995).

4. B. P. Geiser, T. F. Kelly, D. J. Larson, J. Schneir, J. P. Roberts, *Microscopy and Microanalysis* **13**, 437 (2007).

5. F. Vurpillot, G. Da Costa, A. Menand, D. Blavette, *Journal of Microscopy* **203**, 295 (2001).

6. B. Gault, *et al.*, *Journal of Applied Physics* **105**, 034913 (2009).

7. B. Gault, *et al.*, *Ultramicroscopy* **111**, 1619 (2011).

8. M. Ester, H.-P. Kriegel, J. Sander, X. Xu, *et al.*, *kdd* (1996), vol. 96, pp. 226–231.

9. P. Virtanen, *et al.*, *Nature methods* **17**, 261 (2020).

10. S. H. Simon, *The Oxford solid state basics* (OUP Oxford, 2013).

11. F. Vurpillot, A. Bostel, D. Blavette, *Journal of microscopy* **196**, 332 (1999).